Topology Optimization Studies for Light Weight Acoustic Panels

by

Jialian Wu

A thesis submitted in conformity with the requirements for the degree of Masters of Applied Science

Graduate Department of Aerospace Science and Engineering
University of Toronto

Abstract

Topology Optimization Studies for Light Weight Acoustic Panels
Jialian Wu
Master of Applied Science
Graduate Department of Aerospace Science and Engineering
University of Toronto
2016

With the growing need to reduce green house gas emissions, increasing flight efficiency has been a primary challenge faced by the aviation industry. Designing lighter and more efficient aircraft is becoming a goal shared throughout the global air transportation industry. A light weight acoustic panel is desired to replace heavy and bulky foam panels inside the fuselage for cabin noise control. Currently, there is no consensus on the best panel design. Therefore, this thesis will explore using topology optimization to suggest new panel designs. This thesis contains studies of some acoustic panel designs as well as methodologies used to optimize the core topology of a sandwich panel with a maximized band gap while remaining light and stiff. In this thesis, the sound transmission loss has been related to the existence of band gap, and a band gap is being maximized as a surrogate for sound transmission loss. The main results obtained from this thesis show interesting topologies with a band gap around 300 Hz being maximized under mass and stiffness constraints, and the core topologies have been found to have resemblance to resonators.

Acknowledgements

To my heavenly father God, thank you for giving me the bravery and strength to accomplish such a challenging stage of my life.

I would first like to thank my supervisor Professor Craig Steeves, who has provided me essential guidance, endless support, and trust throughout my master thesis. He has inspired me to think and understand my thesis from fundamental aspects, which is a skill that is essential for a researcher. It has been a great opportunity and experience to work with him. Secondly, I would like to thank my RAC committee members, Professor David Zingg and Professor Prasanth Nair, for their instruction during the program. I am also very grateful that my parents and my friends have been providing me emotional and financial support to help me accomplish such a challenging project. I also want to thank all my colleges in the Advanced Aerospace Structures group, who have provided me with an incredible work environment and helped me as much as they can. Lastly, I have to thank my best friend Trefor Evans for his valuable suggestions, discussions, and support to help boost my thesis progress. Lastly, I thank

Contents

List of Figures

List of Tables

Abbreviations

Acronym	Explanation
MMA	Method of Moving Asymptotes
OC	Optimality Criteria
SIMP	Simplified Isotropic Material with Penalization
STL	Sound Transmission Loss

Chapter 1

Introduction

With increasing concern about global warming, which is believed to be largely a result of emissions from the burning of fossil fuels, the International Air Transport Association has set out ambitious industry-wide goals for reducing emissions. Their goal is to have the aircraft industry reach carbon neutral growth by 2020 and to reduce by 50% the total carbon footprint of world air transport by 2050 [15]. With the number of passengers growing every year, it means that a 50% CO_2 reduction per passenger kilometre by 2020 and a 75% reduction by 2050 are required in order to achieve the goals. As a result, minimizing fuel consumption has become a primary challenge for the aircraft industry. Maximizing flight range is analogous to minimizing fuel burn. To address the need to reduce the carbon footprint of aviation, researchers have studied different possibilities to increase fuel efficiency. Given the range equation:

$$R = \left(\frac{\text{Velocity}}{\text{Specific Fuel Consumption}}\right)\left(\frac{\text{Lift}}{\text{Drag}}\right)\ln\left(\frac{\text{Initial Weight}}{\text{Final Weight}}\right), \tag{1.1}$$

feasible solutions to reduce emissions include maximizing the aircraft lift over drag ratio, minimizing the weight of the aircraft, and improving engine efficiency. While other scholars are conducting research to minimize aircraft drag and to increase engine efficiency, structural and material engineers are searching for lighter materials that will meet aircraft application requirements.

A design constraint on aircraft structures is that the noise inside the cabin must be limited. Cabin noise has been identified as a safety issue that can cause headaches, fretfulness, and fatigue in passengers who suffer a constant exposure to it. Moreover, studies have shown that exposure to constant noise can increase passengers' blood

pressure and heart rate [16]. Thus, safety issues related to cabin noise must be considered when designing an aircraft. The current approach is to install large foam panels around the cabin wall to reduce cabin noise. However, they occupy significant volume and make the aircraft heavier [8]. Sandwich structures with carbon fiber composite face sheets and a variety of core topologies are attractive because they can be tailored into high stiffness structures with limited weight penalty. In addition, these structures can be designed to increase sound transmission losses across specific frequency ranges of interest [13, 22, 23]. With advances in 3-dimensional printing technology, fabricating a complex truss topology is feasible. Thus it is of great interest to investigate the possibility of using a sandwich structure as a light weight acoustic panel for the aircraft fuselage.

Various studies have been performed to investigate sandwich structures with assorted core topologies made of carbon fibre composite, foam, or metals, aiming not only to improve acoustic damping but also to increase stiffness to mass ratio [3, 13, 20, 23, 27]. Related studies will be discussed in detail in Chapter 2. From the studies, one can see the potential of porous or truss-like core made of a rapid prototyped polymer being tailored to a specific topology to achieve desired acoustic and structural properties for different applications. Thus, this thesis will study the acoustic performance of sandwich panels with various core topologies in order to maximize sound transmission loss while maintaining low weight and high strength.

1.1 Thesis Objectives

Designing a light weight acoustic panel for aerospace application is a difficult challenge. There is no simple solution for finding an optimized design that can achieve good noise reduction while remaining light and stiff. A substantial amount of effort has been put into increasing sound transmission loss (STL) through the use of multi-layer panels. However, there is no consensus on the best solution. Many related studies are limited to experiments on selected structures. With the infinite possibility of topologies, such an approach is impractical for finding an optimized design. With advances in computational power, it is more feasible to construct numerical approaches to search for the optimal solution. However, the complexity and scale of sandwich structures makes optimization difficult.

The cores of sandwich structures are frequently periodic, composed of repeating

unit cells. Corrugated cardboard is a cheap, common example of such a structure. Making use of the periodicity, one can simplify the acoustic problem by employing Floquet-Bloch analysis to reduce the model size. This approach to modelling enables the relatively inexpensive identification of band gaps in the frequency response of a periodic structure. A band gap is commonly referred to as a stop band, and it is a frequency range in which no plane wave can propagate in any direction. Phani et al [2, 27] have found that the sound transmission loss of a structure increases within its stop band. It is believed that designing a panel that optimizes the frequency gap around unwanted sound frequencies, such as the coincidence frequency at which the sound transmission is the most efficient, decreases the sound transmission through the panel. Thus, being able to maximize the size of the band gap around the targeted frequencies can be useful for many applications where specific frequencies are important. This thesis creates a method to maximize the size of band gaps of a periodic sandwich structure by designing the core using topology optimization. Due to the complexity of the problem, only 2-dimensional configurations are considered.

A literature review is presented in Chapter2. Chapter 3 outlines the formulation of validation problems as well as the thesis problem. The validation results are presented in Chapter 4. Last, the main results for thesis problem are presented in Chapter 5.

Chapter 2

Literature Review

2.1 Aircraft Cabin Noise

Aircraft cabin noise generated from loud engines or high speed flow passing over the fuselage has been identified as a primary source of passenger discomfort during flight travel. Pennig *et al.* [16] have studied the effects of cabin noise on the passenger experience, and they have found that within the audible range, passengers respond more to higher sound pressure, feeling more discomfort. Low frequency sound, from 2 Hz to 35 Hz, although inaudible, can lead to headaches, fretfulness and fatigue [32]. Currently, aircraft manufacturers design for cabin acoustic levels ranging from 50 dB to 110 dB depending on the stage of the flight and type of aircraft [7] [32] and there is no simple solution to produce a cabin structure that can reduce all sources of sound across a broad frequency spectrum.

The most common type of aviation cabin wall consists of a thin aluminum skin over stringers with sound insulating materials between the stringers. New aircraft, such as the Boeing 787, use an ultra light sound-absorbing and heat-insulating melamine resin foam produced by Basotect [8]. Although this type of foam can be as light as 6 kg/m^3, its noise reduction is only effective over the medium to high frequency range (600 Hz to 5000 Hz) [6, 8]. The degree of sound absorbing is only around 10% at 100 Hz for a foam thickness from 20 mm to 100 mm [6]. Therefore, the low frequency sound that causes fatigue remains problematic. In addition, the sound-proofing performance of the foam is highly dependent upon the thickness. A thickness of 50 mm is only effective over frequency ranges from 800 Hz to 5000 Hz, and if the thickness increased to 100 mm, the range of affected frequencies changes to 300 Hz to 5000 Hz. In order

to have better sound-proofing very thick foam is required, filling large volumes and resulting in larger and heavier aircraft.

With the growing application of composite materials to modern aircraft structures, a composite sandwich structure whose core material can be tailored to reduce acoustic noise while maintaining high stiffness and strength has become of great interest. A porous material, honeycomb core, and truss-like cellular solid core have all been shown to have sound reduction effects, ranging approximately from 5 - 10 dB to 20 - 60 dB as frequency increases from 50 Hz to 5000 Hz [2, 3, 13, 20, 22, 23]. The truss-like core in particular has shown its potential for being tailored to a given stiffness and to provide significant sound transmission losses over a targeted frequency range [13, 22, 23]. Subsection 2.3 will introduce various sandwich panel designs with different core topologies and describe their acoustic characteristics.

2.2 Important Acoustic Concepts

In the following section, important equations for acoustic transmission will be introduced, together with a discussion of the acoustic mass law.

2.2.1 Sound wave governing equation and its solution

Assuming the sound propagation process is adiabatic and the wave equation is harmonic time dependent, Newton's law, continuity, and the ideal gas law together give the wave equation as follows:

$$\nabla^2 P = \frac{1}{c_0^2}\frac{\partial^2 P}{\partial t^2} = \frac{\omega^2}{c_0^2}P = k^2 P, \tag{2.1}$$

where P is the pressure, c_0 is speed of sound of the air, t is time, ω is the wave frequency and k is the wave number. A general solution to the plane wave equation for a two dimensional case is given by:

$$p(x, y, t) = Ae^{-ik_x x}e^{-ik_y y}e^{iwt} \ ; \ k^2 = k_x^2 + k_y^2, \tag{2.2}$$

where A is a complex amplitude with the real part representing the magnitude and the imaginary part representing the phase shift, k_x and k_y are the wave numbers in the x and y direction, and i is defined as $\sqrt{-1}$.

2.2.2 Thin plate bending wave equation

A sound wave is transmitted through bending of the plate. The wave pressure excites the plate from the incident side causing bending on the plate, and the bending of the plate excites the particles on both sides and generates a reflected wave on the incident side and a transmitted wave on the other side. For simplicity, the wave propagating direction is restricted to x direction. Figure 2.1 is a 3-dimensional view of the flexural bending waves in a plate subjected to plane wave propagating along the x direction, and Figure 2.2 is a cross-sectional view of the plate.

The equation of motion for the plate subjected to periodic pressure loading $\hat{P}$ is given by [41]:

$$B(1+i\delta)\frac{\partial^4 s}{\partial x^4} + m\frac{\partial^2 s}{\partial t^2} = P(x,t) = \hat{P}e^{i(\omega t - kx)}, \tag{2.3}$$

where s is the transverse plate displacement, m is mass per unit area of the plate, δ is a mechanical loss factor determined by the amount of internal dissipation which converts mechanical energy into thermal energy, and $B = \dfrac{Eh^3}{12(1-\nu^2)}$ is the bending stiffness defined along with plane strain assumption since a thin plate is assumed with parameters E the Young's modulus, h the plate thickness, and ν the Poisson ratio. A general harmonic solution is given as:

$$s = \hat{s}e^{i(\omega t - kx)}, \tag{2.4}$$

where $\hat{s}$ is the magnitude of the transverse plate displacement.

Equation 2.3 can be transformed to become:

$$(B(1+i\delta)k^4 - m\omega^2)\hat{s} = \hat{P}, \tag{2.5}$$

and the above format can be used directly to calculate acoustic impedance introduced below.

2.2.3 Acoustic Impedance

Impedance is defined as a ratio of pressure P over particle velocity u, i.e $Z = \dfrac{P}{u}$. This quantity describes how easily sound can propagate through a medium. Structures with higher impedance have higher sound transmission loss. For a free plane wave travelling

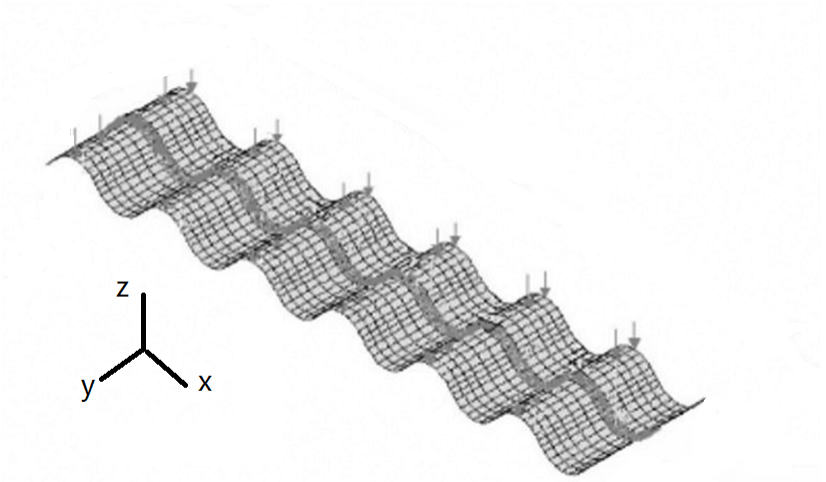

Figure 2.1: Transverse bending wave in a plate subjected to wave propagating along x-direction. Figure is adopted from [17].

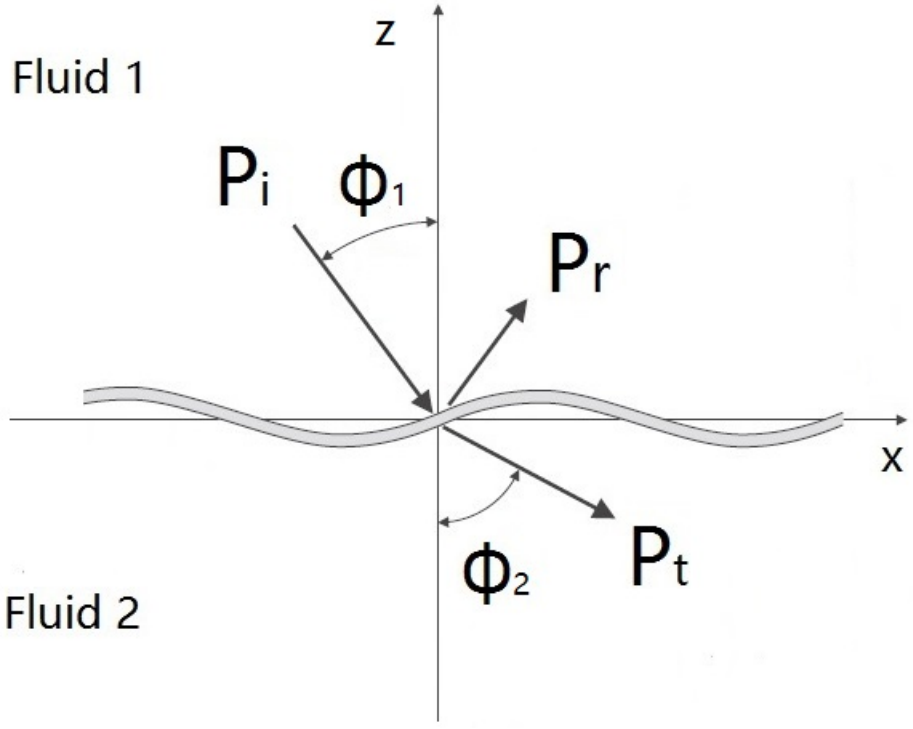

Figure 2.2: Sound propagation through a thin plate with fluid medium 1 on the incident side and fluid medium 2 on the transmission side. P_i is the pressure of incident wave, P_r is the pressure of the reflected wave, and P_i is the pressure of transmitted wave. Incident angle is denoted as ϕ_1, and ϕ_2 denotes transmission angle. Figure is adopted from [41].

in a medium with density ρ and speed of sound c, using Newton's law $-\frac{\partial P}{\partial x} = \rho\frac{\partial u}{\partial t}$, the impedance can be written: $Z = \rho c$. Similarly, for the plate impedance, consider the plane wave equation without damping, i.e $\delta = 0$. The homogeneous solution gives the wave number for the plate as $k_p = (m\omega^2/B)^{1/4}$, and the plate impedance Z_p can be expressed as:

$$Z_p = \frac{P}{\dot{s}} = \frac{\hat{P}}{i\omega\hat{s}} = -i\omega m\left(1 - \frac{k^4}{k_p^4}\right) + \delta\omega m\frac{k^4}{k_p^4}, \tag{2.6}$$

where $\hat{P}$ and $\hat{s}$ are the amplitude of the excitation pressure and transverse plate displacement.

2.2.4 Sound transmission power and transmission loss

Assuming the fluid on both sides is the same, the incident and transmission angles are the same: $\phi_1 = \phi_2 = \phi$. The sound transmission power is defined as:

$$\tau_\pi = \left|\frac{P_t}{P_i}\right|^2 = \left|\frac{2Z}{2Z + Z_p\cos\phi}\right|^2 = \frac{(2\rho c/\cos\phi)^2}{\left[\omega m(1 - (\frac{k_x}{k_p})^4)\right]^2 + \left[\omega m\delta(\frac{k_x}{k_p})^4 + 2\rho c/\cos\phi\right]^2}, \tag{2.7}$$

where P_i is the pressure of the incident wave, and P_t is the pressure of the transmitted wave. Transmission loss is defined as $\mathrm{TL} = 10\log(\tau_\pi^{-1})$. The coincidence frequency occurs when there is a spatial resonance, i.e $k_x = k_p$. As a result, the bending wave and the sound wave become in phase to each other, and the sound transmission is the most efficient and the highest around this frequency. It is given as $\omega_{co} = \sqrt{\frac{m}{B}}\left(\frac{c}{\sin\phi}\right)^2$. The smallest coincidence frequency is also called the critical frequency $\omega_c = \sqrt{\frac{m}{B}}c^2$. It is desirable to increase the critical frequency to avoid resonance of the plate in the lower frequency range which is difficult to attenuate. This can be done by decreasing the stiffness of the structure. By examining Equation 2.7 for limiting values of ω, the general relationship between frequency and impedance can be described. When the excitation frequency is very low, i.e $\omega \ll \omega_{co}$, the mechanical damping term is much less than the mass term. Assuming ω is very small so that $(\omega m\cos\phi) \gg \rho c$, the

transmission loss for plane waves travelling through a thin plate is given as:

$$\omega \ll \omega_{co} \rightarrow \mathrm{TL} = 20 \log \left(\frac{\omega m \cos \phi}{2 \rho c} \right). \tag{2.8}$$

Similarly, transmission loss at higher frequency ranges are given below:

$$\omega \approx \omega_{co} \rightarrow \mathrm{TL} = 20 \log \left(1 + \frac{\delta \omega_{co} m \ \cos \phi}{2 \rho c} \right) \tag{2.9}$$

$$\omega \gg \omega_{co} \rightarrow \mathrm{TL} = 20 \log \left(1 + \frac{B k^4 \sin \phi^4 \cos \phi}{2 \rho c \omega} \right). \tag{2.10}$$

From Equation 2.8 - Equation 2.10, it can be concluded that at very low frequency, the TL is very small, and one way to increase the TL is by increasing the mass of the plate. This is why the transmission loss function is often referred to as the mass law. Alternatively, one can increase the coincidence frequency by decreasing the plate stiffness, which is often undesirable for applications that require strength and stiffness to resist various forces acting on the panel. At higher frequency, the plate stiffness dominates the TL, and when ω approaches ω_{co}, the mechanical loss factor dominates the TL. Since higher frequency sound can be damped by increasing plate stiffness, it is not a major concern. The main challenge is to resolve the conflict between having a light and stiff panel and a low frequency sound barrier. Section 2.3 will present the potential solution to this conflict.

2.3 Acoustic Damping Through Multi-Layer Panels

Because a simple, single plate configuration does not provide sufficient acoustic damping over a wide range of sound frequencies, researchers have been studying multi-layer structures with different core topologies for their acoustic damping effect.

As discussed in section 2.2, higher mass and lower stiffness are desired for increasing transmission loss at low sound frequencies. However in aircraft applications, low stiffness panels are typically not acceptable. Stiff structures, in addition to having low STL at low frequencies, radiate structure-borne sound more efficiently, making their acoustic properties even less desirable [20]. In 1959, Kurtze and Watters [20]

studied sandwich panels to resolve the conflict between having a stiffer structure and achieving higher sound attenuation. They suggested that using a compliant core with stiff face sheets can achieve both higher sound transmission loss and higher stiffness. The following section will discuss research that is related to acoustic damping of multi-layer panels.

2.3.1 Transmission Damping Effect of Porous Media

For acoustic transmission, the internal loss and dissipation on the boundary of the structure is the most significant form of damping. Although the transverse vibration of the plate can be slightly damped when it radiates sound into the air, the combined effect of structural and air damping is not significant. However, when a sound absorbent media is placed next to the plate, a resistive near field is created, which results in significant transmission power loss [33].

Allard [3] studied the sound propagation through porous media by considering the porous layer as an equivalent fluid. He derived acoustic impedance equations for different pore shapes. The acoustic impedance of a porous media depends on the bulk modulus, flow resistivity, porosity, tortuosity, flow density, and the anisotropy factor of the porous material. From Equation 2.7, higher plate impedance results in higher sound transmission loss, so by tailoring the geometry of the porous core in a sandwich panel, it is expected to be able to achieve good sound damping for certain frequency ranges.

2.3.2 Honeycomb Core

Apart from porous media, an anisotropic core, in particular honeycomb core, structure has been shown to provide high STL over a frequency range from around 50 Hz to 5000 Hz. Figure 2.3 is a schematic for a sandwich panel with honeycomb core. Thamburaj and Sun [42] focused on selecting core materials and geometry to transform bending vibration in the top face to shear deformation so that the deformation on the bottom face is minimized. They use a numerical Lagrange-Newton method to optimize the sound transmission loss function subject to stiffness, weight, and thickness constraints. Their results show that anisotropy leads to higher STL. Similar results are obtained by Barton, Mixson, and others [5, 14].

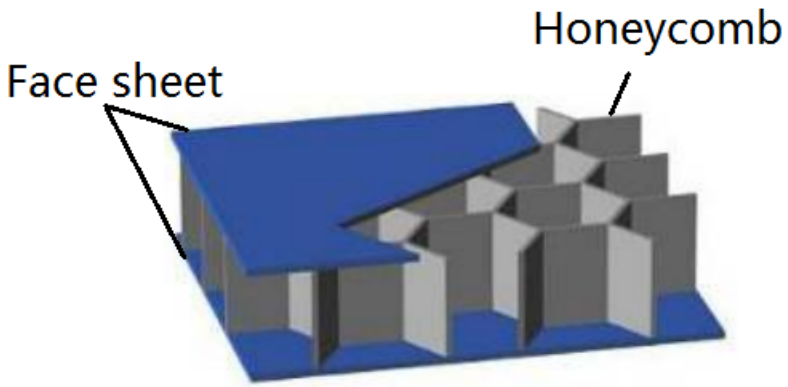

Figure 2.3: Example of a sandwich panel with an anisotropic honeycomb core structure. Figure is adopted from [12].

2.3.3 Truss-like Cellular Solid Core

Recently, there has been a growing interest in sandwich structures with truss-like cellular cores for their amenability to being tailored for specific properties, such as high stiffness, low mass, and good acoustic damping. Ruzzene [22, 34] studied 2-dimensional sandwich beams with the four cellular core topologies shown in Figure 2.4. Each of the four core configurations consisted of a parametrized unit cell; see Figure 2.5. He developed numerical models to calculate the STL for different core structures, and he found that different cellular solid core structures will give significant sound attenuation near some specific frequencies.

Apart from studying the dynamic response of different sandwich panels to obtain desired sound transmission properties, some scholars have approached the problem differently. Because of the periodicity of the cellular truss core, it is possible to consider the structure as similar to a periodic crystal structure, in which case solid state physics can be applied to simplify the analysis of the whole sandwich panel to one repeating unit cell. In 2006, Phani implemented the Floquet-Bloch theorem to analyse plane wave propagation through 2-dimensional periodic structure [2]. Using the Floquet-Bloch theorem, periodic boundary conditions can be applied to the unit cell, and dispersion curves can be obtained by analysing the dynamic response of the unit cell along the edge of the irreducible Brillouin zone. Wave dispersion occurs when plane waves with different frequencies have different propagation speed, and dispersion curves relate the wave number of the travelling wave to its frequency as

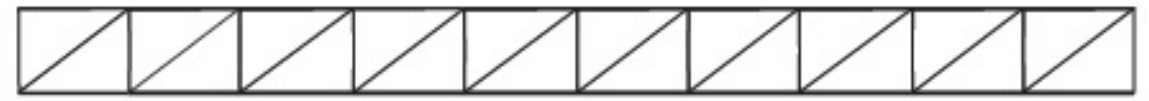

(a) Truss core - square type

(b) Chiral core

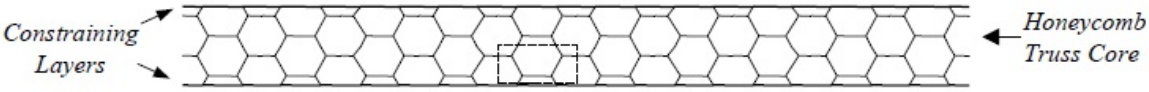

(c) Hexagonal-honeycomb type

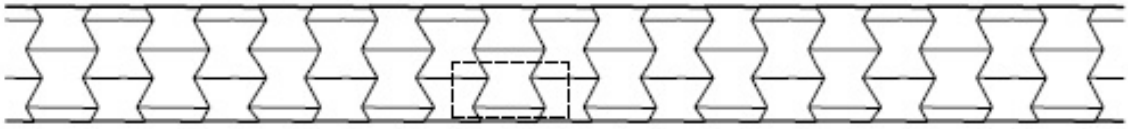

(d) Hexagonal-re-entrant type

Figure 2.4: Cellular solid core topology types being considered by Ruzzene et al [22, 23]. Each structure is constructed by patterning a unit cell over the core region and bound by two face sheets. The unit cells for the four structures are shown in Figure 2.5. Figures are adopted from [22, 23].

shown in Figure 2.6. Details on the Floquet-Bloch theorem and Brillouin zone will be introduced separately in subsection 2.4.1, and details in Phani's approach will be presented in subsection 2.4.2. The main idea is that from the dispersion curves, a band gap indicating the frequency regime through which plane waves cannot propagate can be found. A band-gap is a desirable acoustic property for acoustic damping purposes, since one can control wave propagation through the structure by designing the band gap.

In 2015, Moosavimehr [27] extended Phani's study to a 3-dimensional truss core sandwich panel. He constructed sandwich panels with different truss lattice cores, used ABAQUS to generate the stiffness and mass matrices, applied Phani's approach, and obtained dispersion curves for the sandwich panels. Figure 2.7 shows the different lattice structures with their dispersion curves. For those sandwich panels, there only exist partial band gaps. In Figure 2.7, the dispersion curves for different core topologies have different partial band gap structures near different frequency ranges. For instance,

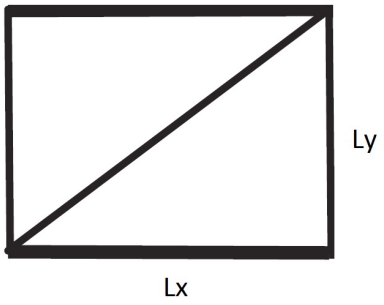

(a) Square unit cell with length and width indicated as Lx and Ly.

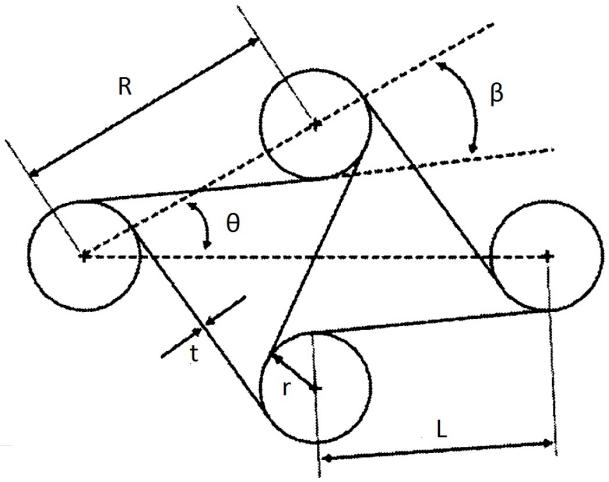

(b) Chiral unit cell with design parameters indicated in the figure.

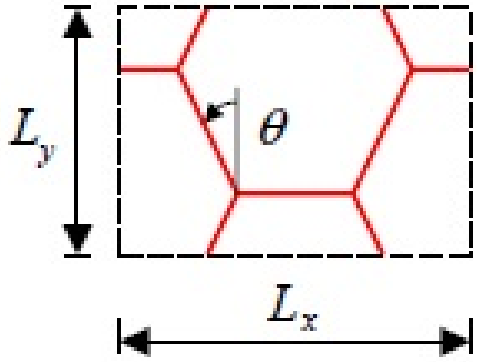

(c) Hexagonal honeycomb unit cell

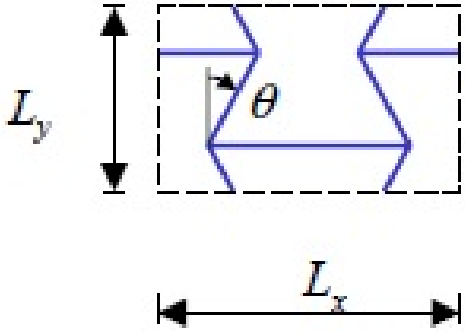

(d) Hexagonal re-entrant unit cell

Figure 2.5: Unit cell for the four structure in Figure 2.4. Each unit cell is parameterized with the design parameters indicated in the graph. Figures are adopted from [22, 23].

the partial band gap near 5 kHz indicated by the grey bar in Figure 2.7b for the tetrahedral lattice core is bigger than the other two structures. As a result,the sound transmission loss of the tetrahedral lattice around 5 kHz is much greater than the other structures as indicated in Figure 2.8. The kagome and pyramidal structures on the other hand has bigger band gap around 2 kHz to 3kHz, and correspondingly, their sound transmission loss near that frequency range is much higher than the tetrahedral structure.

Since directly calculating the STL of an entire sandwich panel has very high computational complexity, it is impractical to design the entire panel. Thus, relating

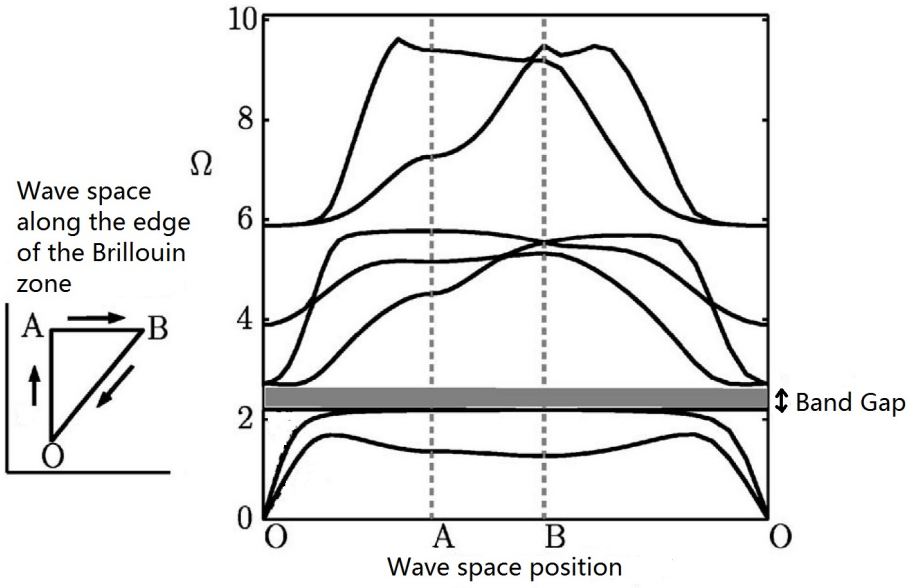

Figure 2.6: Exapmle of dispersion curves for a triangular honeycomb, with the wave space restricted to the edges of the irreducible Brillouin zone, which is the area inclosed by O-A-B-O path. The grey bar indicates the band gap at which no wave can propagate [2]. The wave vector space includes all wave numbers of the plane waves. The Brillouin zone is a reduced wave vector space. Figure is adopted from A.Phani et al. [2].

the existence of band gap to acoustic damping offers a great opportunity for simplifying the design of a whole sandwich panel to the design of a unit cell, making topology optimization of the unit cells of a periodic sandwich panel attractive.

Therefore, this thesis will make use of the periodicity of sandwich panels to optimize STL around specific frequencies by optimizing the band gap around those targeted frequencies. More related literature for proceeding along this path will be introduced in later sections.

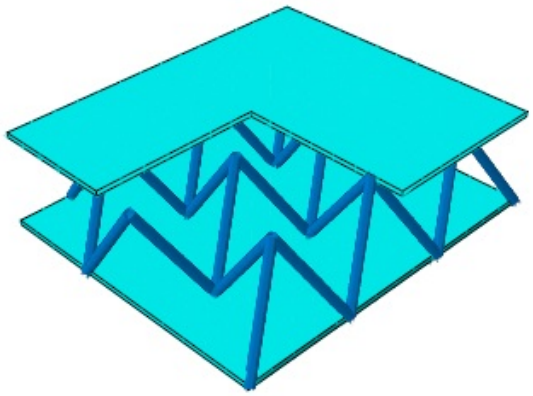

(a) Sandwich panel with tetrahedual lattice Core.

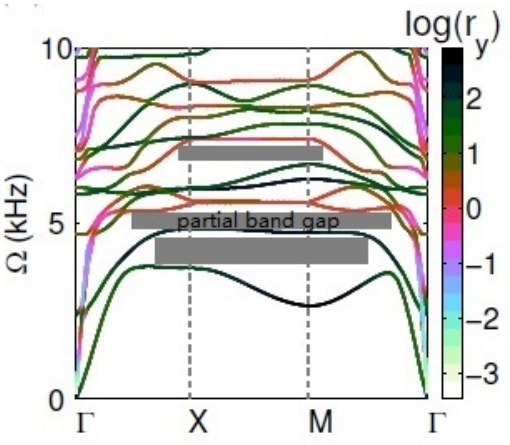

(b) Dispersion curves of tetrahedral lattice core with grey bars indicating some partial band gaps.

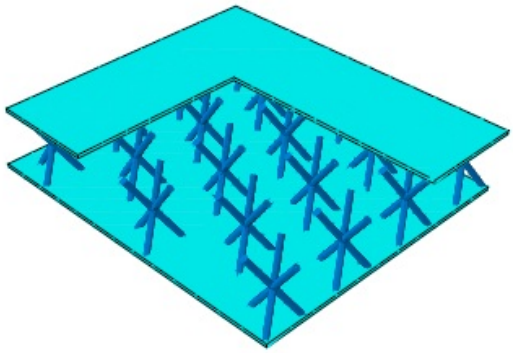

(c) Sandwich panel with kagome lattice core.

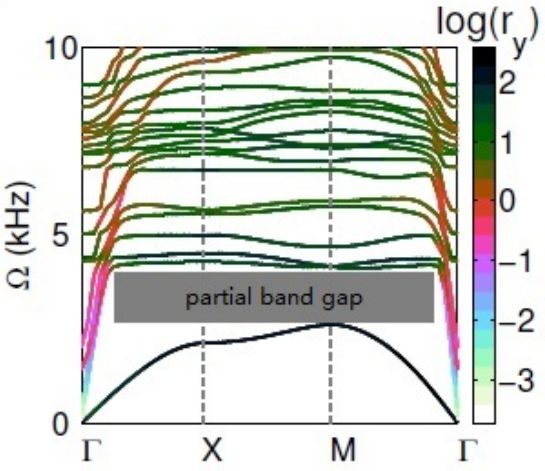

(d) Dispersion curves of kagome lattice core with the grey bar indicating one of the partial band gap around 3 kHz.

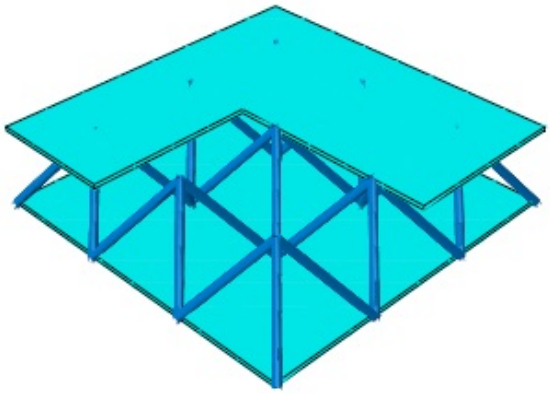

(e) Sandwich panel with pyramidal lattice core

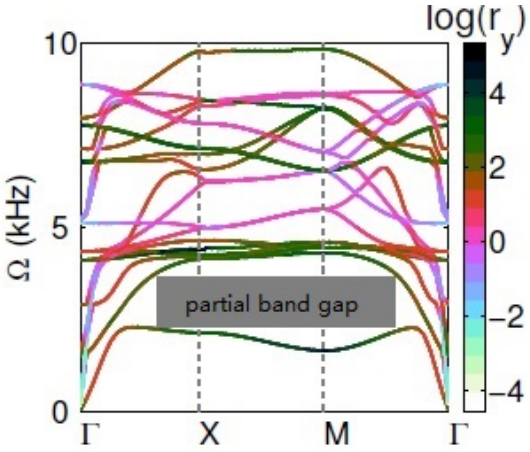

(f) Dispersion curves of pyramidal lattice core with the grey bar indicating one of the partial band gap around 2 kHz.

Figure 2.7: Sandwich panel with different truss lattice core configurations are shown on the left with their corresponding dispersion curves calculated on the right. Figures are adopted from [27].

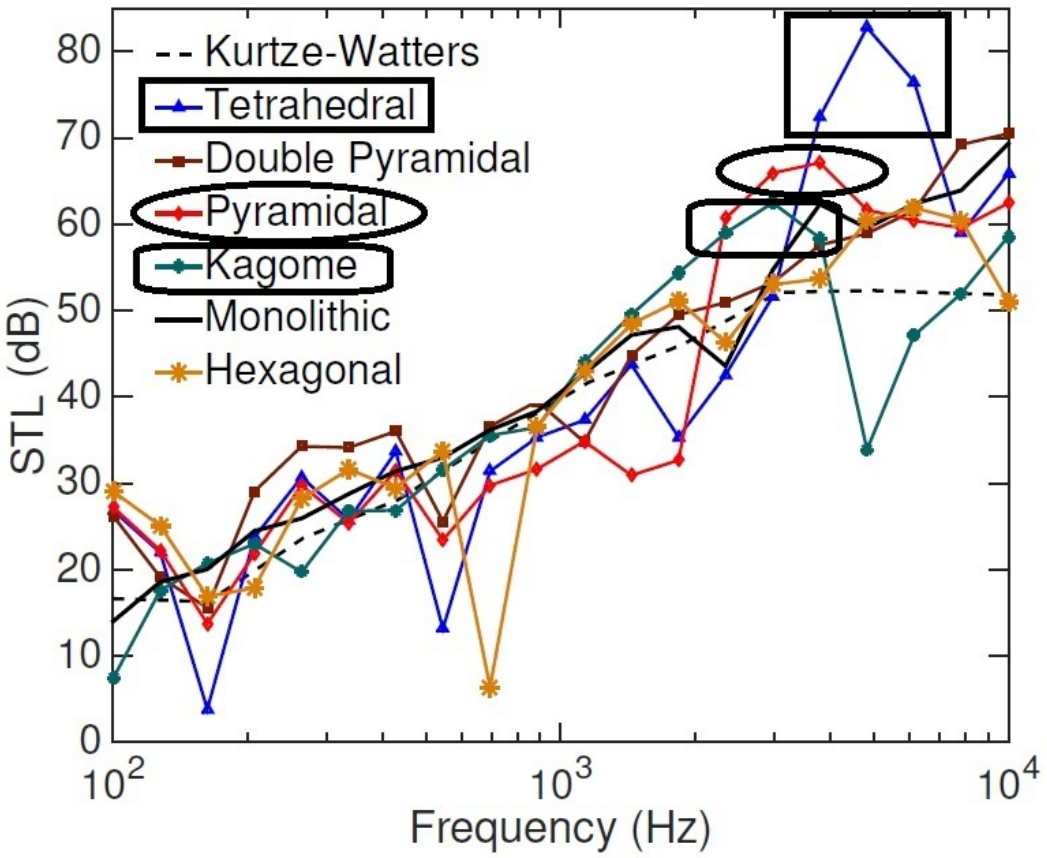

Figure 2.8: Sound transmission loss for various truss lattice core configurations. The x axis indicates the excitation frequency and the y axis is the corresponding STL. The peak STL circled for the three structures correspond to a partial band gap around those frequencies in their band structures shown in Figure 2.7. Figure is adopted from E. Moosavimehr [27].

2.4 Band Gap Calculation for a Periodic Structure

Many periodic structures or materials have been found to exhibit phenomena known as band gaps, which essentially are gaps between two consecutive dispersion curves as shown in Figure 2.6. A positive band gap indicates a frequency regime in which no wave motion can occur. Making use of the band gap characteristic, many scholars performed studies on the dispersion properties of periodic structures or materials to attain a desired band gap for applications in the design of frequency filters, wave guides, beam splitters, etc. [29]. Many of the studies would have encountered great computational complexity without the Floquet-Bloch theorem which allows one to simplify the analysis of a large periodic structure to a representative unit cell. The theorem is of great usefulness for this thesis in order to investigate an optimal band gap of a sandwich structure near desired frequencies. Therefore, this section will introduce the application of the Floquet-Bloch theorem.

2.4.1 The Floquet-Bloch theorem

The governing equations for elastic wave propagation in a three-dimensional homogeneous, isotropic, and elastic medium are presented in Equation 2.11 to Equation 2.13 [29].

$$\rho\frac{\partial^2 u}{\partial t^2} = \frac{\partial}{\partial x}\left(\lambda\nabla\cdot\mathbf{u}\right) + \nabla\cdot\left(\mu\left(\nabla u + \frac{\partial \mathbf{u}}{\partial x}\right)\right), \tag{2.11}$$

$$\rho\frac{\partial^2 v}{\partial t^2} = \frac{\partial}{\partial y}\left(\lambda\nabla\cdot\mathbf{u}\right) + \nabla\cdot\left(\mu\left(\nabla v + \frac{\partial \mathbf{u}}{\partial y}\right)\right), \tag{2.12}$$

$$\rho\frac{\partial^2 w}{\partial t^2} = \frac{\partial}{\partial z}\left(\lambda\nabla\cdot\mathbf{u}\right) + \nabla\cdot\left(\mu\left(\nabla w + \frac{\partial \mathbf{u}}{\partial z}\right)\right), \tag{2.13}$$

where $\mathbf{u} = \{u\ v\ w\}$ is the displacement vector, λ and μ are Lame's coefficients, and ρ is the density of the material.

The Floquet-Bloch theorem states that when elastic waves propagate through a periodic structure without attenuation, the complex wave amplitude in a repeating unit cell does not depend on the location of the cell in the whole structure [2]. In another words, it is adequate to study the wave motion within a unit cell in order to capture the wave behaviour of the whole structure. Elastic waves that are attenuated cannot propagate at all. A mathematical expression for the Floquet-Bloch theorem is

given as the solution to Equation 2.11 through Equation 2.13 possessing the following periodicity:

$$\mathbf{u}\left(\mathbf{r},t\right)=\mathbf{u}_{k}\left(\mathbf{r},t\right)e^{(\mathbf{k}\cdot\mathbf{r}-iwt)}, \tag{2.14}$$

where $\mathbf{u}_k$ is the displacement field of the unit cell, $\mathbf{r}$ is the location vector of the unit cell, $\mathbf{k}$ is the wave vector, and w is the angular frequency. Inserting Equation 2.14 into the governing equations and solving the partial differential equations using the finite element method to be introduced in section 2.5, the general form of the problem can be obtained

$$\left(\mathbf{K}\left(\mathbf{k}\right)-w^{2}\mathbf{M}\right)\mathbf{u}=\mathbf{f}, \tag{2.15}$$

where $\mathbf{K}$ and $\mathbf{M}$ are the global stiffness and mass matrices respectively, and $\mathbf{f}$ is the force vector.

2.4.2 Floquet Bloch Applications in Calculating the Dispersion Curves

A more explicit form of Equation 2.15 is introduced by Phani [2]. By constructing the stiffness and mass matrix of the unit cell directly without considering the Floquet-Bloch periodic boundary conditions, one arrives at the assembled form of the governing equations Equation 2.11 to Equation 2.13.

$$\left(\mathbf{K}-w^{2}\mathbf{M}\right)\mathbf{u}=\mathbf{f}, \tag{2.16}$$

where $\mathbf{K}$ and $\mathbf{M}$ are the stiffness and mass matrices, $\mathbf{u}$ is the displacement vector, and $\mathbf{f}$ is the force vector.

By virtue of the Floquet-Bloch theorem, the displacement, $\mathbf{u}$, and force, $\mathbf{f}$, possess the following properties:

$$\begin{cases} \mathbf{u}_i &= \mathbf{u}_i \\ \mathbf{u}_r &= e^{k_x}\mathbf{u}_l \\ \mathbf{u}_t &= e^{k_y}\mathbf{u}_b \\ \mathbf{u}_{rb} &= e^{k_x}\mathbf{u}_{lb} \\ \mathbf{u}_{lt} &= e^{k_y}\mathbf{u}_{lb} \\ \mathbf{u}_{rt} &= e^{k_x+k_y}\mathbf{u}_{lb} \\ \mathbf{f}_r &= -e^{k_x}\mathbf{f}_l \\ \mathbf{f}_t &= -e^{k_y}\mathbf{f}_b \\ \mathbf{f}_{rt} + e^{k_x}\mathbf{f}_{lt} + e^{k_y}\mathbf{f}_{rb} + e^{k_x+k_y}\mathbf{f}_{lb} &= 0 \end{cases}, \tag{2.17}$$

where the subscripts $l,\ r,\ t,\ b$ indicate left, right, top, and bottom, i indicates internal nodes, and the double subscript indicates the corner elements. See Figure 2.9 for an illustration. The key consequence of this is that the displacements of locations on the boundary of the unit cell have specific relations to one another.

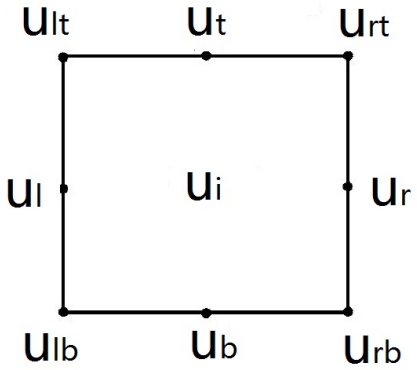

Figure 2.9: Node labelling of a 2-dimensional square repeating unit cell with edges connected to neighbouring unit cells.

A transformation matrix constructed by applying the above relations is used to convert the displacement from the Bloch reduced coordinate to the complete coordinate, such that $\mathbf{u} = \mathrm{T}\tilde{\mathbf{u}}$, where

$$\tilde{\mathbf{u}} = \begin{bmatrix} u_l & u_b & u_{lb} & u_i \end{bmatrix}^T, \tag{2.18}$$

is the Bloch reduced coordinate and

$$\mathbf{T} = \begin{bmatrix} \mathbf{I} & 0 & 0 & 0 \\ \mathbf{I}e^{k_x} & 0 & 0 & 0 \\ 0 & \mathbf{I} & 0 & 0 \\ 0 & \mathbf{I}e^{k_y} & 0 & 0 \\ 0 & 0 & \mathbf{I} & 0 \\ 0 & 0 & \mathbf{I}e^{k_x} & 0 \\ 0 & 0 & \mathbf{I}e^{k_y} & 0 \\ 0 & 0 & \mathbf{I}e^{k_y+k_x} & 0 \\ 0 & 0 & 0 & \mathbf{I} \end{bmatrix}, \tag{2.19}$$

is the transformation matrix.

By substituting $\mathbf{u} = \mathbf{T}\tilde{\mathbf{u}}$ into Equation 2.16 and pre-multiplying the equation with the Hermitian transpose $\mathbf{T}^{\mathrm{H}}$, the governing equation in the Bloch reduced coordinate system is obtained:

$$\mathbf{T}^{\mathrm{H}} \left(\mathbf{K} - w^2\mathbf{M}\right) \mathbf{T}\tilde{\mathbf{u}} = \mathbf{T}^{\mathrm{H}}\tilde{\mathbf{f}}. \tag{2.20}$$

The solution to the above eigenvalue problem depends on the wave propagating frequency w and wave number vector (k_x, k_y), where the wave numbers are complex values with the real part representing sound attenuation and the imaginary part representing the phase angle. The eigenfrequency is a function of the wave vector. For each pair of k_x and k_y, a set of eigenvalues and eigenvectors are generated, with the eigenvalues indicating the natural frequencies of the structure under the wave motion with wave numbers k_x and k_y along the x and y direction, and with the eigenvectors representing the mode shapes of the structure at those frequencies. For all wave vectors, the eigenfrequencies of the eigenproblem form solution surfaces, also known as dispersion surfaces. If two consecutive surfaces do not have any frequency values crossing each other, then there exists a band gap between the two surfaces, see Figure 2.6 for illustration. Inside the band gap, no wave mothon can occur. The concepts of reciprocal unit in wave vector space is widely used in solid state physics to transform a problem from time space to frequency space through a Fourier transformation. With the transformation, the problem become easier to solve in the

wave vector space. For convenience, the basis vectors for the direct and reciprocal cells are set to satisfy the following relation [2]:

$$\mathbf{e}_i \cdot \mathbf{e}_j^* = \delta_{ij}, \tag{2.21}$$

where $\mathbf{e}_i$ are the basis vectors for the direct cell and $\mathbf{e}_j^*$ are the basis vectors for the reciprocal cell. For a square unit cell, the basis vectors for the direct and reciprocal cell align with each other, and for more complex lattices, the details can be found in [2]. To solve the problem, at least two of the unknowns must be provided. These are chosen to be the two components of the wave vector propagating along the direction of the basis vectors of the reciprocal unit. The wave vector space still has infinite possible combinations. It has not yet been directed. The space can be reduced to discrete space thanks to the periodicity of the structure [19]. The reduced space is the Brillouin zone and is also a Wigner-Seitz unit cell of the reciprocal lattices, which can be constructed by selecting one lattice point, connecting it to all neighbouring points, and constructing the perpendicular bisects of those lines to form a closed region, as shown in Figure 2.10. It is computationally expensive to search the entire

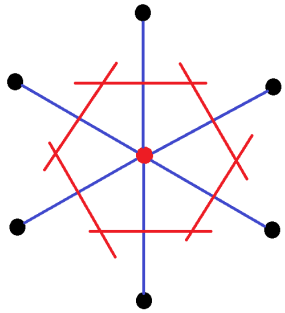

Figure 2.10: Construction of Brillouin zone of the reciprocal unit cell with all the dots indicating lattice points. Region enclosed by red lines is the Brillouin zone.

Brillouin zone to construct complete dispersion curves. If the lattice has symmetry, the Brillouin zone can be reduced to a unique region which is a subset of the cell and is referred to as the irreducible Brillouin zone, see Figure 2.11 for example. To reduce the computational complexity, the wave vectors are often restricted to the edges of the irreducible part of the first Brillouin zone, indicated as the Γ - X - M - Γ path in Figure 2.11, to explore band gaps since the band extrema, at which the change of eigenfrequencies with respect to the change of wave vector is zero and thus the group

velocity of plane waves is zero, almost always occur on the boundaries of the Brillouin zone according to Kittel [19].

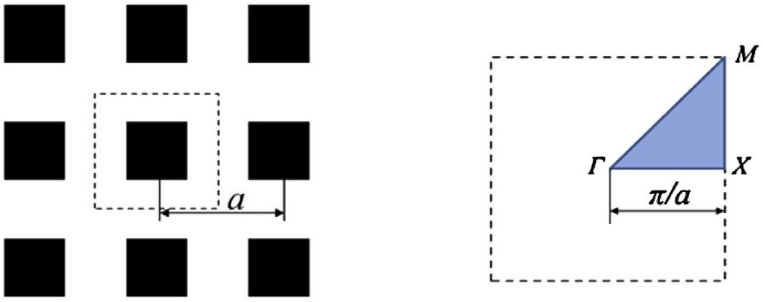

Figure 2.11: Figure on the left is a unit cell with square symmetry. The blue section in the figure on the right indicates the irreducible part of the Brillouin zone for the unit cell. The three pivots are labeled as Γ, X, and M [11].

For a square unit cell with square symmetry, if waves are propagating without attenuation and the wave vector is purely imaginary, the wave constants k_x and k_y at the three pivots, denoted as Γ, X, and M, of the irreducible Brillouin zone are given as:

$$\begin{aligned} &\Gamma\,(0,0) \\ &X\left(i\frac{\pi}{a},0\right) \\ &M\left(i\frac{\pi}{a},i\frac{\pi}{a}\right), \end{aligned}$$

where i indicates complex number, and a is the base length of the unit cell.

To sum up, the dispersion curves are calculated by solving the eigenproblem of Equation 2.20 along the edges of the irreducible Brillouin zone, and the band gap is found between two consecutive dispersion surfaces that do not have any frequency value crossing each other.

2.5 Finite Element Analysis

The band-gap analysis for a structure with arbitrary topology will not be possible to achieve in a practical manner without a finite discretization. This is because the

governing Equations 2.11 to 2.13 are partial differential equations without known solutions. The main steps in the finite element analysis involve discretizing the design domain into small elements, representing the elements with shape functions, and constructing the global stiffness and mass matrices of the whole structure. Since the finite element strategies are very well-known, details are presented in Appendix A.

2.6 Topology Optimization

Topology optimization is an effective way to search for an efficient material layout within a design domain for desired physical performance, such as high stiffness, high acoustic damping and high natural frequency. It is done by distributing allowable material throughout the design domain to achieve an optimal value of an objective function. In practise, topology optimization is commonly used to generate early stage conceptual designs that have the most desirable properties and meet specified design constraints. The optimal topology obtained from the method is then improved further for better performance and manufacturability often by using shape optimization, which is a structural optimization method that optimizes the shape of the structure [1]. The difference between topology and shape optimization is that the former optimizes the topology as well as the shape of a structure, for instance creating holes, while the later optimizes the shape or the holes without changing the topology. For industrial applications, manufacturing constraints are often required to achieve structures that meet specific manufacturing requirements [10]. For the scope of this thesis, only an early stage model will be developed with a limited number of constraints.

Topology optimization relies on iterative analysis and design update steps, and gradient based analysis is often used for guiding the searching direction. There exist many topology optimization methods, and a review is given by Sigmund and Maute [30]. The topology optimization method that is implemented in this thesis is the "density method", which divides the design domain into many elements and optimizes the topology by determining the density of each element. By assigning a density value of 0 or 1 to each element, the allowable material is distributed to favour an optimal objective function. However, the discrete nature of the problem imposes difficulty for sensitivity analysis, making it impractical to solve topology optimization problems that often consist of large sets of design variables. Continuous density variables are more favourable since gradient-based optimization can be used to search for an optimal

solution more efficiently. However, non-physical intermediate density elements are impermissible. In order to prevent intermediate density and encourage 0-1 solutions, the Simplified Isotropic Material with Penalization (SIMP) approach was introduced by Bendsoe in 1989 [28]. The approach suggested penalization to intermediate density by modifying the material property in the following way:

$$E\left(\rho_e\right) = \rho_e^p E_0, \tag{2.22}$$

where ρ_e is the density of element e, p is the penalty value usually set to 3, and E_0 is the Young's modulus of solid material. The penalization scheme is only effective when volume constraints are imposed, since under volume constraint, a 0-1 solution will be more effective compared to an intermediate solution. In this thesis, the density method will be used in conjunction with the SIMP approach to solve the optimization problem considered here. The optimization scheme used to solve the density-based topology problem is introduced in the following section.

2.6.1 Optimization Scheme

Density based topology optimization is often done by dividing the structure into many discrete elements and optimizing the density of each element to achieve the desired structure. These types of optimization problem are often non-linear, implicit, and have a large sets of design variables and constraints. Traditional optimization methods, such as steepest descent method, are usually too slow to be practical for performing such an optimization.

In 1987, Svanberg proposed a generalized version of the convex linearisation (CONLIN) method to solve structural optimization problems, named the method of moving asymptotes method (MMA). MMA is based on a conservative convex separable approximation (CCSA) which is widely used in many other optimization algorithms, such as sequential quadratic programming. The method constructs a sub-problem that is convex and separable to replace the primary implicit and non-linear problem. Convex approximation ensures the sub-problem to be solved has a unique solution equivalent to the primary solution. Approximating separability makes the procedure more efficient when solving for the Lagrange multipliers. Due to the characteristics of the approximation, MMA can handle problems with a large number of design variables and constraints.

2.6.1.1 Method of Moving Asymptotes

Consider the general structural optimization problem having the following form

$$\begin{array}{lll} \text{Problem : minimize} & f_0(\mathbf{x}) & (\mathbf{x} \in R^n) \\ \text{Subject to :} & f_i(\mathbf{x}) \leq \hat{f}_i & \text{for} \quad i = 1, ..., m \ , \\ \text{and} & x_{\min} \leq x_j \leq x_{\max} & \text{for} \quad j = 1, ..., n \end{array} \tag{2.23}$$

where f_0 is the objective function, $f_i(\mathbf{x}) \leq \hat{f}_i$ are behavioural constraints such as stresses and displacements, and $x_{\min}$ and $x_{\max}$ are the bounds on the design variables x_j.

The MMA solves the optimization problem by generating and solving an explicit sub-problem in an iterative manner. The iteration steps are listed below.

1. Given an initial guess $\mathbf{x}_0$ at iteration $k = 0$.

2. At each iteration k, calculate the objective function $f_0\left(\mathbf{x}^k\right)$, the constraint function $f_i\left(\mathbf{x}^k\right)$ and their derivatives $\nabla f_0\left(\mathbf{x}^k\right)$ and $\nabla f_i\left(\mathbf{x}^k\right)$.

3. Construct the sub-problem $P^{(k)}$ by replacing the implicit functions f_i with the approximating explicit function $g_i^{(k)}$ based on calculations obtained from the previous step.

4. Solve for the optimal solution to the sub-problem and use it to adjust the approximation function and to perform another internal iteration l within the outer iteration k, until $g_i^{(k,l)}\left(\mathbf{x}^{(k,l)}\right) \geq f_i^{(k)}\left(\mathbf{x}^{(k)}\right)$. Let the solution $\left(\mathbf{x}^{(k,l)}\right)$ be the next iteration point $\mathbf{x}^{(k+1)}$. Continue the iterations until convergence criteria are met or when the user is satisfied with the solution.

The approach for constructing the approximating explicit function $g_i^{(k,l)}$ and the sub-problem $P^{(k)}$ are detailed in [39] [40]. The method will be introduced without detailed explanations here.

For each iteration k, the design variable x_j are bounded by a lower limit L_j and a upper limit U_j, which are also refered to as the moving asymptotes:

$$L_j^{(k)} \leq x_j^{(k)} \leq U_j^{(k)}. \tag{2.24}$$

The approximation functions $g_i^{(k,l)}$ are defined such that they are both convex and separable, given as:

$$g_i^{(k,l)}(\mathbf{x}) = r_i^{(k,l)} + \sum_{j=1}^{n} \left(\frac{p_{ij}^{(k,l)}}{U_j^{(k)} - x_j} + \frac{q_{ij}^{(k,l)}}{x_j - L_j^{(k)}} \right), \tag{2.25}$$

where

$$p_{ij}^{(k,l)} = \begin{cases} \left(U_j^{(k)} - x_j^{(k)}\right)^2 \dfrac{\partial f_i}{\partial x_j} + \dfrac{\rho_i^{(k,l)} \sigma_j^{(k)}}{4} & \text{if} \quad \dfrac{\partial f_i}{\partial x_j} > 0 \\ 0 & \text{if} \quad \dfrac{\partial f_i}{\partial x_j} \leq 0 \end{cases}, \tag{2.26}$$

$$q_{ij}^{(k,l)} = \begin{cases} 0 & \text{if} \quad \dfrac{\partial f_i}{\partial x_j} \geq 0 \\ -\left(x_j^{(k)} - L_j^{(k)}\right)^2 \dfrac{\partial f_i}{\partial x_j} + \dfrac{\rho_i^{(k,l)} \sigma_j^{(k)}}{4} & \text{if} \quad \dfrac{\partial f_i}{\partial x_j} < 0 \end{cases}, \tag{2.27}$$

and

$$r_i^{(k,l)} = f_i\left(\mathbf{x}^{(k)}\right) - \sum_{j=1}^{n} \left(\frac{p_{ij}^{(k,l)}}{U_j^{(k)} - x_j^{(k)}} + \frac{q_{ij}^{(k,l)}}{x_j^{(k)} - L_j^{(k)}} \right). \tag{2.28}$$

For the above equations, all derivatives are evaluated at $\mathbf{x} = \mathbf{x}^{(k)}$, and the moving asymptotes have the following relations to the design variable:

$$L_j^{(k)} = x_j^{(k)} - \sigma_j^{(k)} \qquad \text{and} \qquad U_j^{(k)} = x_j^{(k)} + \sigma_j^{(k)}, \tag{2.29}$$

where $\sigma^{(k)}$ is given as:

$$\begin{cases} \sigma^{(k)} &= \text{asy}_{init}\left(x_j^{\max} - x_j^{\min}\right) & \text{for} \quad k < 3 \\ \sigma^{(k)} &= \gamma_j^{(k)} \sigma_j^{(k-1)} & \text{for} \quad k \geq 3 \end{cases}, \tag{2.30}$$

where asy_{init} is used to tune the move limit in the first two iterations and is usually assigned with value 0.5, and γ is given as:

$$\gamma = \begin{cases} \text{asy}_{decr} & \text{if} \quad \left(x_j^{(k)} - x_j^{(k-1)}\right)\left(x_j^{(k-1)} - x_j^{(k-2)}\right) < 0 \\ \text{asy}_{incr} & \text{if} \quad \left(x_j^{(k)} - x_j^{(k-1)}\right)\left(x_j^{(k-1)} - x_j^{(k-2)}\right) > 0 \\ 1 & \text{if} \quad \left(x_j^{(k)} - x_j^{(k-1)}\right)\left(x_j^{(k-1)} - x_j^{(k-2)}\right) = 0 \end{cases}, \tag{2.31}$$

where asy_{incr} and asy_{decr} are called the asymptote increase and asymptote decrease values that can be adjusted by the user for specific problems to increase the rate of convergence. The suggested values are 1.2 and 0.7.

The updating of the parameter ρ is

$$\begin{array}{rcll} \rho_i^{(1,0)} & = & 1 & \\ \rho_i^{(k+1,0)} & = & \max\left\{0.1\rho_i^{\left(k,\tilde{l}(k)\right)}, \rho_i^{\min}\right\} & \\ \rho_i^{(k,l+1)} & = & \min\left\{10\rho_i^{(k,l)}, 1.1\rho_i^{(k,l)} + \delta_i^{(k,l)}\right\} & \text{if} \quad \delta_i^{(k,l)} > 0 \\ \rho_i^{(k,l+1)} & = & \rho_i^{(k,l)} & \text{if} \quad \delta_i^{(k,l)} \leq 0 \end{array}, \tag{2.32}$$

where $\tilde{l}\,(k)$ is the total number of inner loops in the k iteration, and δ_i is given as:

$$\delta_i^{(k,l)} = \frac{f_i\left(\mathbf{x}^{(k)}\right) - g_i\left(\mathbf{x}^{(k,l)}\right)}{\frac{1}{2}\sum_{j=1}^{n} \frac{\left(\left(\mathbf{x}^{(k)}\right) - \left(\mathbf{x}^{(k,l)}\right)\right)^2}{\sigma_j^2 - \left(\left(\mathbf{x}^{(k)}\right) - \left(\mathbf{x}^{(k,l)}\right)\right)^2}}. \tag{2.33}$$

With the above approximation to the functions f_i at each iteration, the sub-problem is guaranteed to be convex and separable, and thus a dual method can be used to solve the sub-problem. Details on the dual method can be found in reference [40] . Applying the dual method, the sub-problem is constructed as:

$$\begin{array}{lll} \text{Sub-problem:} & \min\limits_{\mathbf{x}} g_0^{(k)}(\mathbf{x}) + a_0 z + \sum\limits_{i=1}^{m}\left(c_i y_i + 0.5 d_i y_i^2\right) & \\ \text{Subject to :} & g_i^{(k)}(\mathbf{x}) - a_i z - y_i \leq 0, & i = 1, ..., m \\ & \min_x \leq x_j \leq \max_x, & j = 1, ..., n \\ & y \geq 0, \quad z \geq 0 & \end{array}, \tag{2.34}$$

where y is the vector of Lagrange multipliers also called the dual variable, and z is an artificial variable that is introduced to prevent bad initial points that often lead to infeasible solutions. The coefficients a_i, c_i, and d_i can be adjusted to solve different optimization problems.

2.7 Sensitivity Analysis

Gradient based optimization relies on the derivatives of the objective and constraint functions with respect to all design variables in order to search in the right direction. Since the aim of this thesis is to optimize the gaps in the frequency band structure of a sandwich panel, the objective function will contain eigenvalues generated from the eigenproblem introduced in previous section. Lacking explicit differentiability, sensitivity analysis for eigenvalues is often done by using a mathematical perturbation technique. The following section will introduce the detailed methodology along with the sensitivity analysis for compliance.

2.7.1 Derivatives of Eigenvalues

Eigenvalues represent the natural frequencies of the system. In most cases, each eigenvalue corresponds to an eigenvector, which represents the mode shape of the eigensystem. Calculating sensitivities for these cases is relatively straightforward. However, for complex structures that have many design parameters and many degrees of freedom, for instance stiffener-reinforced thin-walled plate and shell structures, a dense spectrum of eigenvalues is often expected, and thus eigenvalues with multiplicity are often found in those structures [4]. In addition, symmetry of the structure can generate linearly independent buckling modes and vibration modes having eigenvalues with multiplicity [4]. Here, the multiplicity is considered when the numerical differences between eigenfrequencies are within a small tolerance. The structures considered in this thesis share those charateristics that exist when multiple eigenvalues are expected, thus the multiplicity of eigenvalues must be addressed. Seyranian [4] introduced techniques to calculate both simple and multiple eigenvalues based on mathematical perturbation analysis of the eigenvalues and their corresponding eigenvectors. The following will outline the methodology.

The sensitivity calculation for a simple eigenvalue is:

$$\frac{d\lambda_i}{dx_j} = \Phi_i^T \left(\frac{\partial \mathbf{K}}{\partial x_j} - \lambda_i \frac{\partial \mathbf{M}}{\partial x_j} \right) \Phi_i, \tag{2.35}$$

where λ_i is the i^{th} eigenvalue, Φ_i is the corresponding eigenvector, x_j is the j^{th} design variable, and $\mathbf{K}$ and $\mathbf{M}$ are the global stiffness and mass matrices generated by the

finite element method. The eigenvectors are normalized by:

$$\Phi_i^T \mathbf{M} \Phi_i = \mathbf{I}, \tag{2.36}$$

where $\mathbf{I}$ is the identity matrix.

When there exist eigenvalues with N multiplicity, the sensitivity analysis is not straightforward since the eigenvectors for the multiple eigenvalues are not unique. Any linear combination of the eigenvectors will be a solution to the original eigenproblem, and the sensitivity analysis of the multiple eigenvalues has to be treated differently to take into account the non-unique eigenvectors. To do so, Seyranian [4] suggested constructing a generalized gradient vector $\mathbf{f}_{sk}$ such that

$$\mathbf{f}_{sk} = \left(\Phi_s^T \left[\frac{\partial \mathbf{K}}{\partial x_1} - \tilde{\lambda} \frac{\partial \mathbf{M}}{\partial x_1} \right] \Phi_k, ..., \Phi_s^T \left[\frac{\partial \mathbf{K}}{\partial x_n} - \tilde{\lambda} \frac{\partial \mathbf{M}}{\partial x_n} \right] \Phi_k \right), \quad \text{for} \quad s = 1, ..., N; \quad k = 1, ..., N \tag{2.37}$$

where n is the number of design variables, N is the multiplicity of the eigenvalue, and $\tilde{\lambda}$ is the repeating eigenvalue. The sensitivity is obtained by solving the following problem:

$$\det \left[\mathbf{f}_{sk}^T \mathbf{e} - \mu \delta_{sk} \right] = 0, \quad s, k = 1, ..., N, \tag{2.38}$$

where $\mathbf{e}$ is the direction vector for the design variables, μ is the sensitivity, and δ_{sk} is the Kronecker delta. The problem in Equation 2.38 is not as simple to solve as it first appears since the direction vector $\mathbf{e}$ is undetermined for the problem. Pedersen interpreted Seyranian's work in a more useful form [31]. Considering a double eigenvalue case only, we have eigenvalue λ^2 and its corresponding eigenvectors $\{\Phi_1\}$ and $\{\Phi_2\}$. Any linear combination of the two eigenvectors will be an eigenvector with the same eigenvalue.

$$\left\{ \bar{\Phi} \right\} = c_1 \{\Phi_1\} + c_2 \{\Phi_2\} \tag{2.39}$$

$$c_1^2 + c_2^2 = 1 \Rightarrow \left\{ \bar{\Phi} \right\}^T M \left\{ \bar{\Phi} \right\} = 1. \tag{2.40}$$

By inserting Equation 2.39 into Equation 2.35 gives

$$\frac{d\lambda}{dx} = c_1^2 g_{11} + c_2^2 g_{22} + 2c_1 c_2 g_{12} \tag{2.41}$$

$$g_{nm} = \{\Phi\}_n^T \left(\frac{\partial \mathbf{K}}{\partial x_j} - \lambda_i \frac{\partial \mathbf{M}}{\partial x_j} \right) \{\Phi\}_m . \tag{2.42}$$

To find the extreme values of Equation 2.41, differentiate Equation 2.41 with respect to c_1 and c_2 and get

$$\begin{bmatrix} g_{11} & g_{12} \\ g_{21} & g_{22} \end{bmatrix} \begin{Bmatrix} c_1 \\ c_2 \end{Bmatrix} = \begin{Bmatrix} 0 \\ 0 \end{Bmatrix} \tag{2.43}$$

Solving the eigenproblem for the matrix in Equation 2.43 gives the eigenvectors c_a and c_b with their corresponding eigenvalues g_a and g_b. As quoted from Pedersen "For multiple eigenvalues, the sensitivity is given for two specific directions in the space of eigenvectors and these eigenvectors will vary for different design parameters," which means that the two sensitivities, g_a and g_b, are not always the sensitivities to the design variables since the direction of the design space can vary. A more sophisticated way to arrive at the sensitivity is by iteration implemented by Du and Olhoff [18], but that is computationally expensive.

The proposed approach by the author is introduced here. By an educated guess, we want be to able to interpolate the sensitivity between the two extreme values. By making use of the coefficients c_a and c_b, we can construct an eigenvector as in Equation 2.39, use this new eigenvector along with c_a and c_b to construct the sensitivity of the same form in Equation 2.41:

$$\left\{ \frac{d\lambda}{dx} \right\}_a = \begin{bmatrix} g_{a11} & g_{a12} \\ g_{a21} & g_{a22} \end{bmatrix} \begin{Bmatrix} c_{a1} \\ c_{a2} \end{Bmatrix}, \tag{2.44}$$

with

$$g_{anm} = \left\{ \bar{\Phi} \right\}_n^T \left(\frac{\partial \mathbf{K}}{\partial x_j} - \lambda_i \frac{\partial \mathbf{M}}{\partial x_j} \right) \left\{ \bar{\Phi} \right\}_m \tag{2.45}$$

$$\left\{ \bar{\Phi} \right\} = c_{a1} \{\Phi_1\} + c_{a2} \{\Phi_2\} . \tag{2.46}$$

The above $\left\{ \frac{d\lambda}{dx} \right\}_a$ will be the sensitivity for the relatively lower eigenvalue, and

similarly using c_b to calculate $\left\{\frac{d\lambda}{dx}\right\}_b$ for the relatively higher eigenvalue. Although not found in any literature, the above method has been shown to have good agreement with finite difference approximations in practise. However, since topology optimization is always trying to optimize the density of the unit cell, it has been noticed that there is a minimum density limit to this approach for it to perform well, and that has been tested to be around $\rho = 0.001$. The proposed method has been tested on topology optimization problems only, and for other problems, the accuracy is not guaranteed.

2.7.2 Derivatives of Compliance

The sensitivity for compliance can be calculated directly since the compliance is given as :

$$c(\mathbf{x}) = \mathbf{U}^T\mathbf{K}\mathbf{U} = \sum_{e=1}^{N} x_e^p \mathbf{u}_e^T \mathbf{k}_e \mathbf{u}_e, \tag{2.47}$$

where p is the suggested penalty value by SIMP approach, $\mathbf{u}_e$ is the displacement vector, and $\mathbf{k}_e$ is the element stiffness matrix. The sensitivity thus is given as:

$$\frac{\partial c}{\partial x_e} = -p\,(x_e)^{p-1}\,\mathbf{u}_e^T \mathbf{k}_e \mathbf{u}_e. \tag{2.48}$$

2.7.2.1 Mesh Independent Filtering Technique

Due to the fact that checkerboard geometry with elements alternating between 0 and 1, could appear to be a stiff structure numerically but is not a physically meaningful design, a filtering technique is introduced by Sigmund to prevent these types of structures [36]. The mesh independent filtering technique is done by modifying the sensitivities by the following equation:

$$\frac{\partial \hat{c}}{\partial x_e} = \frac{1}{x_e \sum_{f=1}^{N} \hat{H}_f} \sum_{f=1}^{N} \hat{H}_f x_f \frac{\partial c}{\partial x_f}, \tag{2.49}$$

where

$$\hat{H}_f = r_{min} - \mathrm{dist}(e, f) \quad \{f \in N \mid \mathrm{dist}(e, f) \leq r_{min}\}, \quad \text{for} \quad e = 1, ..., N. \tag{2.50}$$

The operator dist (e, f) indicates the distance between element e and f, making the convolution operator $\hat{H}_f$ to be zero outside of the filter area. The filter size indicated as r_{min} is used to determined which neighbour elements to be filtered. Typical values of the filter radius are set from 1.1 to 1.5, assuming the size of the unit cell is 1. However, such a filtering technique often leads to intermediate densities along the boundaries, which is not desired. Post-processing is often required to further address those intermediate densities.

Chapter 3

Problem Formulation and Code Construction

In order to verify the accuracy of the algorithm implemented by the author, three different problems are constructed to check the performance of the code. The first problem is to minimize the compliance of an infinite sandwich beam with a volume constraint. The second problem is to minimize the minimum eigenvalue of a beam clamped at both ends, whose result will be compared to work done by other scholars. The third problem is a band gap optimization problem for photonic material considered by Sigmund, and the result will be compared to the existing one. Finally, the formulation of the thesis problem, which is to optimize the band gap of a 2-dimensional periodic sandwich beam, will be presented.

This chapter outlines the problem formulation and code construction of the three verification problems as well as of the proposed thesis problem. Chapter 4 presents the verification results for the three problems, and Chapter 5 presents the main results obtained for this thesis.

3.1 Compliance Optimization Problem

The problem being considered here is an infinite 2-dimensional periodic sandwich beam subjected to uniform shear loading on the top plate while being constrained at the bottom plate, and due to the periodicity, only a unit cell is modelled as indicated in Figure 3.1. The applied loading and boundary conditions are assigned such that the sandwich beam is subjected to simple shearing, and thus only the shear stiffness is

being optimized in this problem. The unit cell has two face sheets with predetermined thickness, and the core is to be designed through topology optimization process so that minimum shear compliance can be achieved.

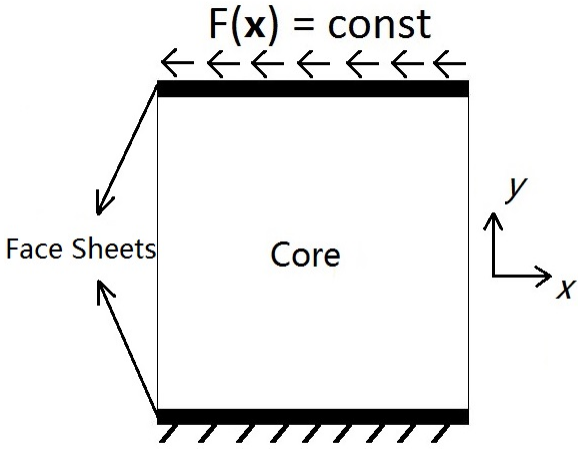

Figure 3.1: A unit cell for a 2-dimensional periodic sandwich beam with two face sheets and the core indicated in the figure. The unit cell is constrained at the bottom face with uniform shear force acting at the top face.

The optimization problem is formulated as:

$$\begin{array}{lll} \text{Problem :} & \min\limits_{\mathbf{x}} c\left(\mathbf{x}\right) = \mathbf{U}^T\mathbf{K}\mathbf{U} = \sum_{j=1}^{N} x_j^p \mathbf{u}_j^T \mathbf{k}_j \mathbf{u}_j & \left(\mathbf{x} \in R^n\right) \\ \text{Subject to :} & \text{Volume Fraction}\left(\mathbf{x}\right) = \sum_{j=1}^{N} x_j \leq V_{max} & \\ & \mathbf{K}\mathbf{U} = \mathbf{F} & \\ & 0.001 \leq x_j \leq 1 & \text{for} \quad j = 1, ..., N \end{array} , \tag{3.1}$$

where p is the penalization factor for the SIMP method, V_{max} is the maximum allowable volume density, and N is the total number of design variables. The number of design variables corresponds to the total number of elements in the finite element analysis. The corresponding coefficients to be used for the sub-problem as discussed in section 2.6 are set as $a_0 = 1$, $a_1 = 0$, $d_1 = 1$, and $c_1 = 1000$ [37]. The main structure of the code is shown in Figure 3.2.

In step 1, the initial guess is provided as a uniformly distributed structure with the density of each core element equal to the maximum allowable average volume

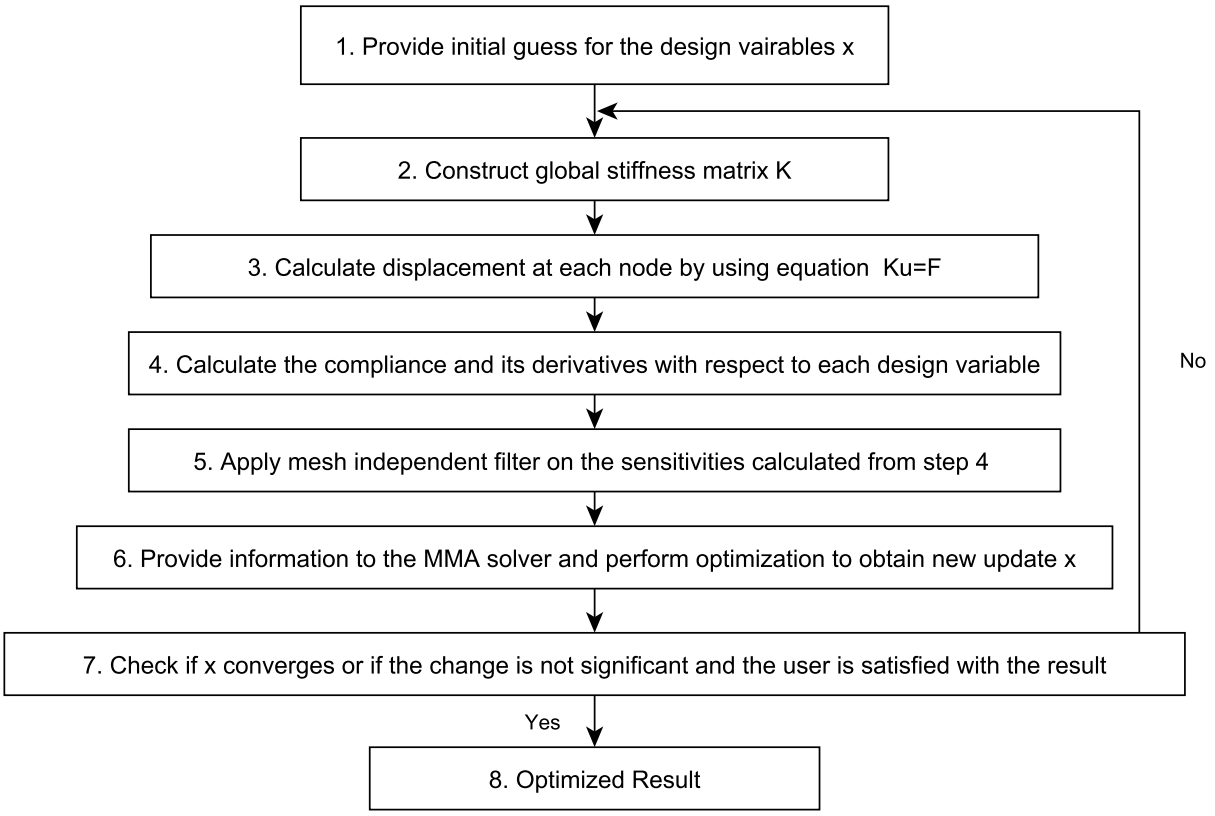

Figure 3.2: Flow chart of the iterative optimization process for minimizing compliance.

Element Type	E	ρ
Face Sheet	70GPa	3 kg/m^3
Core	10GPa	1 kg/m^3

Table 3.1: Element material properties

density. In step 4, the compliance and derivatives are calculated using total equations introduced in subsection 2.7.2. As suggested by Svanberg, it is preferable to scale the constraints and objective function in a way that $1 \leq f_i^{max} \leq 100$, and the design variable is better to be scaled to let $0.1 \leq x_{max} - x_{min} \leq 100$. Step 5 uses the mesh independent filtering technique introduced in subsubsection 2.7.2.1. The information required to perform optimization in step 6 is in the MMA code `mmasub.m` writen by Svanberg in 1995 [38]. The optimization code is build on `mmasub.m` with modification done by the author according to his new 2002 version [39]. The core is discretized into `nelx` by `nely` elements along the x and y direction indicated in the figure. The material properties for the plate and core elements are listed in Table 3.1. The material properties for face sheets and core correspond approximately to aluminum and polymer.

3.2 Maximizing the Minimum Eigenfrequency

The problem considered here is the same as the one considered by Du and Olhoff [18], where the minimum eigenfrequency is being maximized for a beam clamped at both ends, see Figure 3.3.

Since the MMA only minimizes the objective function, it is necessary to use the

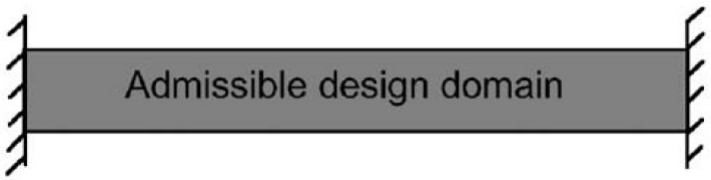

Figure 3.3: Beam constrained at both ends. Figure is adopted from Du and Olhoff [18].

reciprocal of the eigenvalue to turn the max-min problem into a min-max problem, i.e minimizing the maximum of the reciprocal of the eigenvalue. A standard formation of the problem is shown below.

$$\begin{array}{lll} \text{Problem :} & \min\limits_{\mathbf{x}} \max \left\{ \dfrac{1}{\lambda_i(\mathbf{x})} \right\} & (\mathbf{x} \in R^n) \\ \text{Subject to :} & \sum\limits_{j=1}^{n} x_j \leq V_{\max} & \\ & \Phi_i^T \left(\mathbf{K} - \lambda_i(\mathbf{x}) \mathbf{M} \right) \Phi_i = \mathbf{0} \quad \text{for} \quad i = 1, ..., J & \\ & \Phi_i^T \mathbf{M} \Phi_m = \delta_{im} \qquad \text{for} \quad i, m = 1, ..., J & \\ & x_{\min} \leq x_j \leq x_{\max} \qquad \text{for} \quad j = 1, ..., n & \end{array} , \tag{3.2}$$

where J is the number of eigenvalues being considered, n is the number of design variables, $V_{\max}$ is set at 0.5, $x_{\min}$ is 0.001, and $x_{\max}$ is 1.

The MMA solves the following problem:

$$\begin{array}{lll} \text{Sub-problem:} & \min\limits_{\mathbf{x}} g_0^{(k)}(\mathbf{x}) + a_0 z + \sum\limits_{i=1}^{m} \left(c_i y_i + 0.5 d_i y_i^2 \right) & \\ \text{Subject to :} & g_i^{(k)}(\mathbf{x}) - a_i z - y_i \leq 0, & i = 1, ..., m \\ & x_{\min} \leq x_j \leq x_{\max}, & j = 1, ..., n \end{array} . \tag{3.3}$$

The min-max problem can be equivalently written as

$$\begin{array}{lll} \text{Sub-problem:} & \min\limits_{\mathbf{x}} \quad z & \\ \text{Subject to :} & \dfrac{1}{\lambda_i(\mathbf{x})} - a_i z \leq 0, & i = 1, ..., J \\ & \sum\limits_{j=1}^{n} x_j \leq V_{\max} & \\ & \Phi_i^T \left(\mathbf{K} - \lambda_i(\mathbf{x}) \mathbf{M} \right) \Phi_i = \mathbf{0} \quad \text{for} \quad i = 1, ..., J & \\ & \Phi_i^T \mathbf{M} \Phi_m = \delta_{im} \qquad \text{for} \quad i, m = 1, ..., J & \\ & x_{\min} \leq x_j \leq x_{\max} \qquad \text{for} \quad j = 1, ..., n & \end{array} , \tag{3.4}$$

with the corresponding coefficients for the sub-problem being set as $a_0 = 1$, $a_i = 1$ for $i = 1, ..., J$, $a_i = 0$ for $i = J+1, ..., M$, $d_i = 1$, and $c_i = 1000$ [37], where M is the

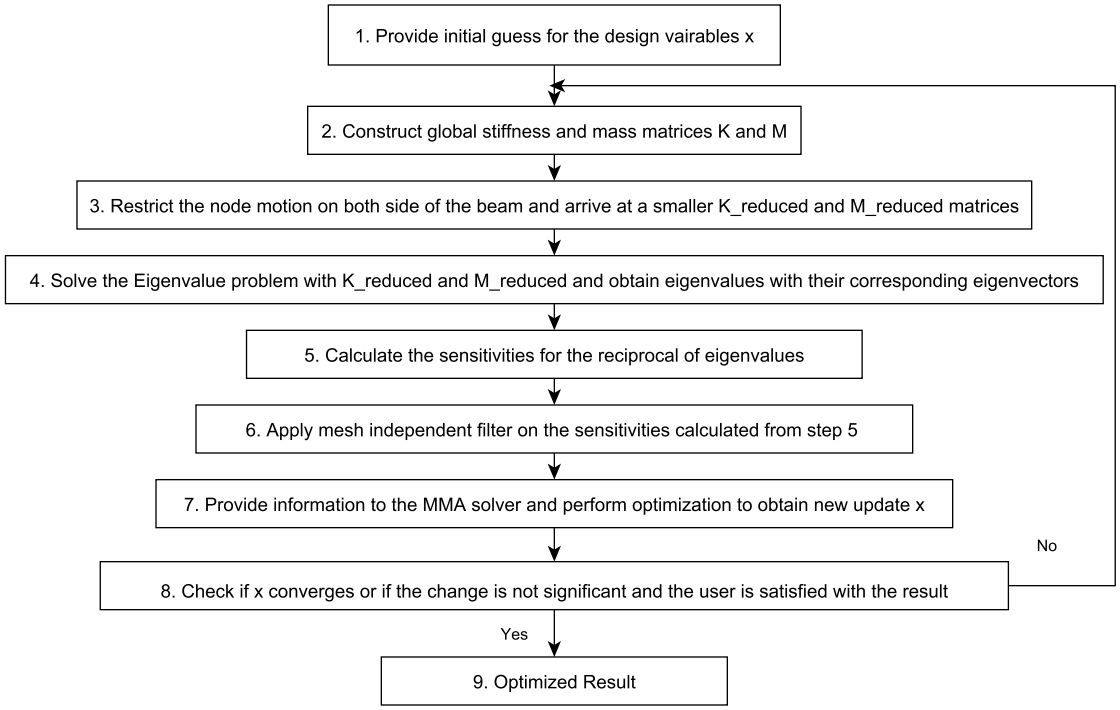

Figure 3.4: Flow chart of the iterative optimization process for maximizing the minimum eigenvalue.

total number of constraints. The two approaches give similar results, but the second form is used to keep the problem formulation consistent with Du and Olhoff.

The main structure of the optimization code is shown in Figure 3.4. At the start, all available material is uniformly distributed throughout the design space. The stiffness and mass matrices constructed in step 2 use a different penalty scheme to avoid spurious or localized modes occurring near low density elements with $x_j < 0.1$. When the element has low density, the ratio between the stiffness and mass matrix becomes very small, generating spurious modes. As suggested by Du and Olhoff [18], the following penalty scheme is used to ensure a C^0 or C^1 continuity of the interpolation model.

$$\mathbf{K} = \sum_{j=1}^{N} x_j^p \mathbf{K}_j, \quad \mathbf{M} = \begin{cases} x_j \mathbf{M}_j & x_j > 0.1 \\ (c_0 x_j^6)\mathbf{M}_j & x_j \leq 0.1 \quad \text{with } C^0 \text{ continuity} \\ (c_1 x_j^6 + c_2 x_j^7)\mathbf{M}_j & x_j \leq 0.1 \quad \text{with } C^1 \text{ continuity} \end{cases}, \tag{3.5}$$

where $c_0 = 10^5$, $c_1 = 6 \times 10^5$, $c_2 = -5 \times 10^6$, and p is the penalty, set to 3. Since the beam is clamped at both ends, there is a need to eliminate the inactive degrees of freedom from the global $\mathbf{K}$ and $\mathbf{M}$ matrices which is done in step 3. Step 4 is straightforward; however, the eigenvectors must be normalized. Step 5 is for calculating the gradient of the constraint functions. Since the problem is formulated in such a way that no objective function f_0 is used, it will be set to 0. The gradient for the reciprocal of the eigenvalue is calculated using analytical differentiation:

$$\frac{d\left\{\frac{1}{\lambda}\right\}}{dx} = -\frac{1}{\lambda^2}\frac{d\lambda}{dx}. \tag{3.6}$$

The sensitivity is filtered using Sigmund's method introduced in [36]. Note that it is slightly different from the one introduced in another paper by Sigmund [35].

The program will exit when a convergence criteria is met or when the user is satisfied with the result. In this thesis, the program will exit when the change over an iteration is smaller than a threshold. This threshold will vary when different asymptotes or move limits are used.

3.3 Band Gap Optimization

In 2003, Sigmund and Jenson [29] had studied elastic wave propagation of photonic band-gap material. The photonic band-gap material consists of two different types of material that have different material properties. They studied different cases with multiple material combinations under in-plane and out-of-plane stress, and one of those cases will be reconstructed here in order to perform validation for the algorithm developed in this thesis. The properties of the materials to be considered are listed in Table 3.2.

Material	E	ρ	ν
Type a	20GPa	2 kg/m^3	0.34
Type b	4GPa	1 kg/m^3	0.34

Table 3.2: Properties of the two materials with high contrast in Young's modulus.

The problem is to distribute those two materials throughout the design domain so that a band gap of maximum size is achieved. As claimed by Sigmund [29], there is no need to impose a volume constraint for one of the materials since a pure phase material does not exhibit band gap phenomena. There are no other types of constraint imposed for this problem.

Consider the band gap equation:

$$\text{Band Gap} = 2\frac{\min\{\lambda_{b+1}(\mathbf{k})\} - \max\{\lambda_b(\mathbf{k})\}}{\min\{\lambda_{b+1}(\mathbf{k})\} + \max\{\lambda_b(\mathbf{k})\}}, \tag{3.7}$$

where the band gap is calculated between the b^{th} and the $(b+1)^{th}$ band, and $\mathbf{k}$ are wave vectors along the boundaries of the irreducible Brillouin zone. Since the eigenvalues in Equation 3.7 are a function of the wave vector $\mathbf{k}$, it is possible for the minimum point of the $(b+1)^{th}$ band and the maximum point of the b^{th} band to change wave vector location during the iteration. Therefore, only using the current minimum and maximum points to represent the objective function is not comprehensive because the next minimum and maximum points could be at different locations. As suggested by Meng et al [11], the band gap equation needs to be modified with weight functions. The assumptions used to determine the weight functions are:

- Any eigenfrequency from $(b+1)^{\text{th}}$ to the Jth frequency, the maximum frequency being considered, that are less than $c_2 = 1.1 \times \min\left\{\sqrt{\lambda_{b+1}(\mathbf{k})}\right\}$ has the possibility of becoming the next minimum point of the $(b+1)^{\text{th}}$ band.

- Similarly any eigenfrequency from the first to the b^{th} eigenvalue that are greater than $c_1 = 0.9 \times \max\left\{\sqrt{\lambda_b(\mathbf{k})}\right\}$ has the possibility of becoming the next maximum point of the b^{th} band.

See Figure 3.5 for illustration. The optimization problem is then formulated:

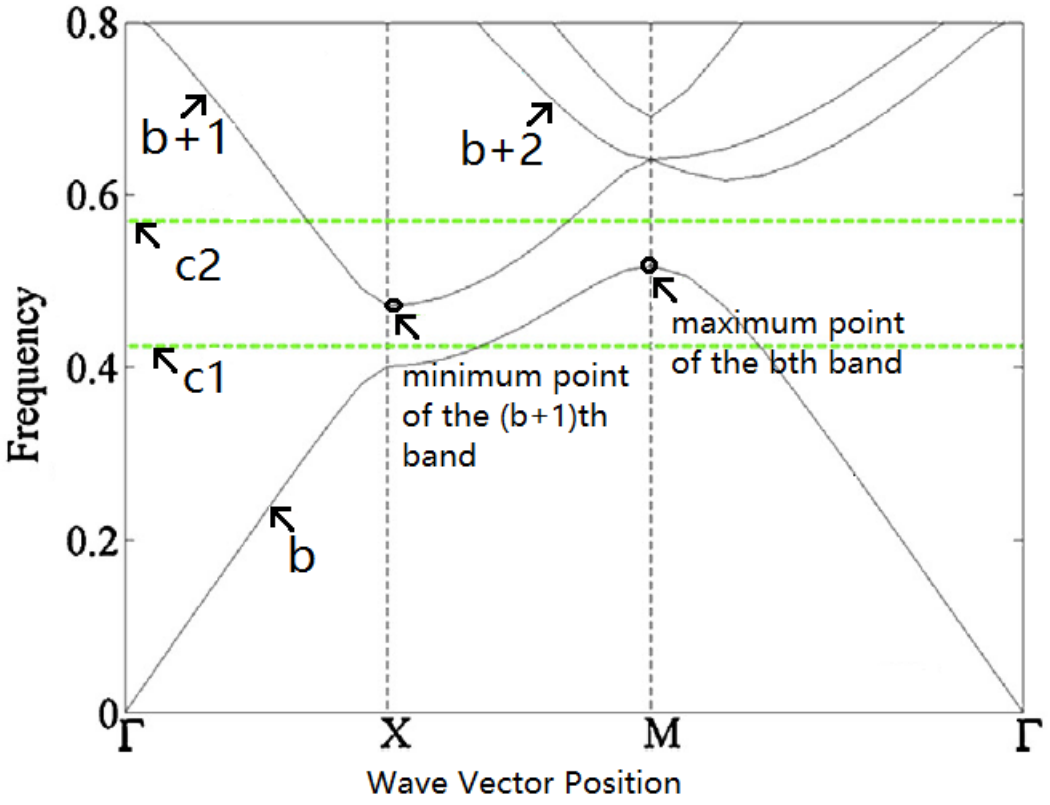

Figure 3.5: The current maximum and minimum points are indicated in the figure at their corresponding wave vector positions. Any frequency on the $b+1$ th band or above that is below the top green line has the potential to become the next minimum point. Any frequency on the (b)th band and lower that is above the bottom green line has the potential to become the next maximum point. Figure is adopted from [11].

$$\text{Sub-problem:} \quad \min_{\mathbf{x}} \quad \frac{1}{\text{Band Gap}} = \frac{\sum_{l=1}^{Q}\sum_{i=b+1}^{J} w_{li}\lambda_i(\mathbf{k}_l) + \sum_{l=1}^{Q}\sum_{i=1}^{b} \hat{w}_{li}\lambda_i(\mathbf{k}_l)}{\sum_{l=1}^{Q}\sum_{i=b+1}^{J} w_{li}\lambda_i(\mathbf{k}_l) - \sum_{l=1}^{Q}\sum_{i=1}^{b} \hat{w}_{li}\lambda_i(\mathbf{k}_l)}$$

$$\begin{aligned} \text{Subject to :} \quad & \Phi_i^T \mathbf{T}^H \left(\mathbf{K} - \lambda_i(\mathbf{x})\mathbf{M}\right)\mathbf{T}\Phi_i = \mathbf{0} && \text{for} \quad i = 1, ..., J \\ & \Phi_i^T \mathbf{T}^H \mathbf{M}\mathbf{T}\Phi_m = \delta_{im} && \text{for} \quad i, m = 1, ..., J \\ & 0.001 \le x_j \le 1 && \text{for} \quad j = 1, ..., N \end{aligned} \tag{3.8}$$

where Q is the length of the irreducible Brillouin zone, J is the highest eigenvalue to be calculated, $\mathbf{T}$ is the transformation matrix constructed using the Floquet-Bloch theorem, and w_{li} or $\hat{w}_{li}$ are the weighted coefficients suggested by Meng et al[11] given below:

$$\begin{aligned} w_{li} &= \frac{A_{li}}{\sum_{l=1}^{Q}\sum_{i=b+1}^{J} A_{li}} \\ \hat{w}_{li} &= \frac{\hat{A}_{li}}{\sum_{l=1}^{Q}\sum_{i=1}^{b} \hat{A}_{li}} \end{aligned}, \tag{3.9}$$

with

$$\begin{aligned} A_{li} &= \begin{cases} c_2 - \sqrt{\lambda_i(\mathbf{k}_l)} & \text{when } \sqrt{\lambda_i(\mathbf{k}_l)} < c_2 \\ 0 & \text{otherwise} \end{cases} \quad l = 1, ..., Q; i = b+1, ..., J \\ \hat{A}_{li} &= \begin{cases} \sqrt{\lambda_i(\mathbf{k}_l)} - c_1 & \text{when } \sqrt{\lambda_i(\mathbf{k}_l)} > c_1 \\ 0 & \text{otherwise} \end{cases} \quad l = 1, ..., Q; i = 1, ..., b \end{aligned} . \tag{3.10}$$

The optimization procedure for the problem is given in Figure 3.6. In step 1, the initial design is given in Figure 3.7, and the unit is discretized into a 30x30 grid. For step 5, the sensitivities for the eigenvalues are calculated individually using the method outlined in subsection 2.7.1, and those are used to calculate the gradient of the objective function following differentiation rules. Again, the problem will exit when the change in the design parameter drops below a threshold set by the user.

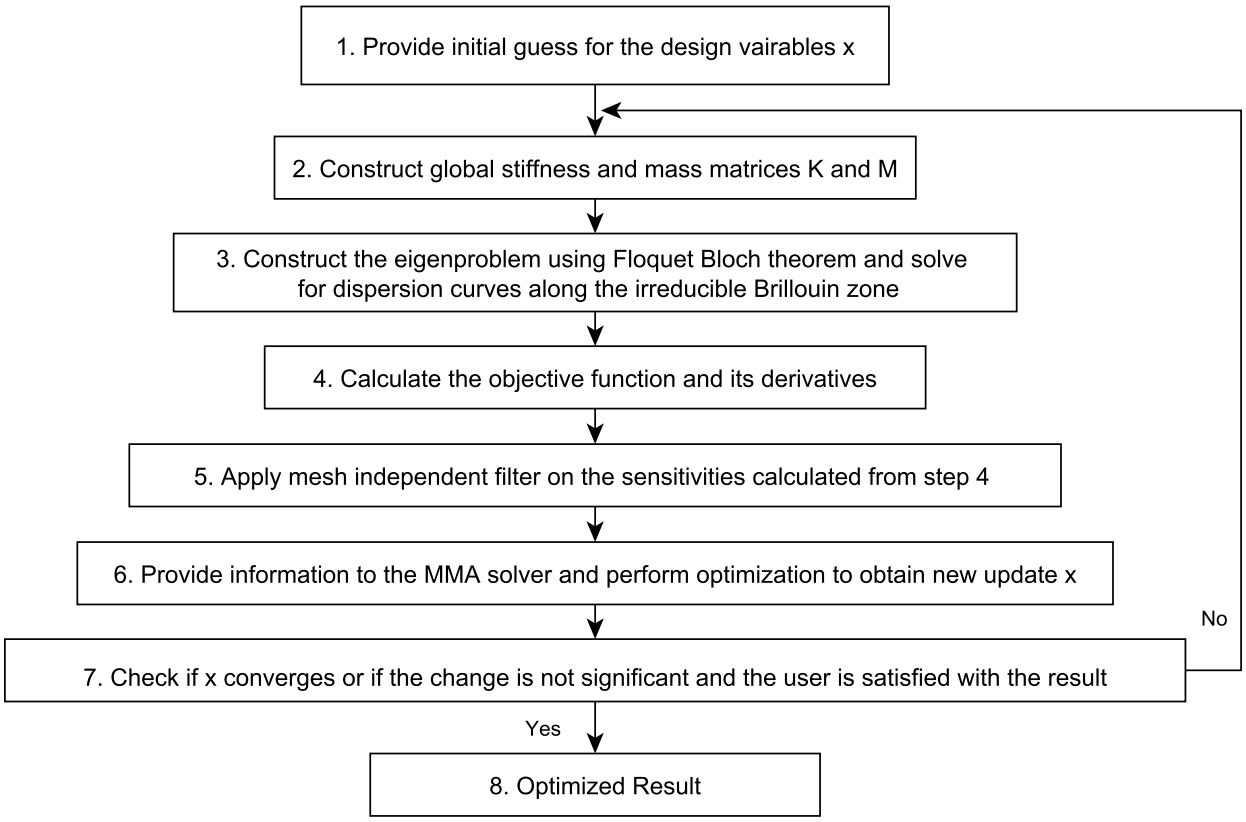

Figure 3.6: Iterative optimization procedure for optimizing the band gap of a photonic material.

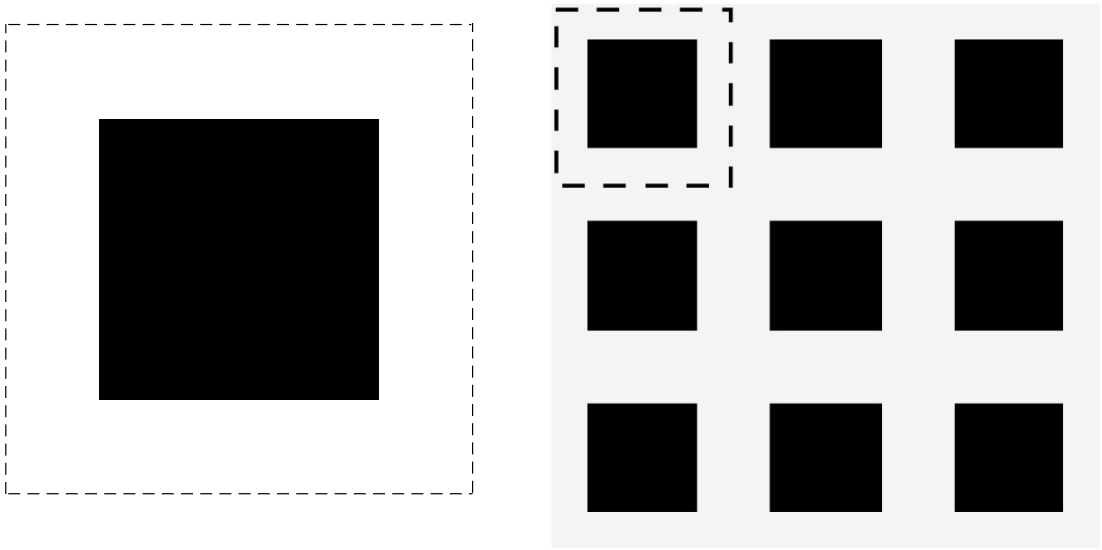

(a) A unit cell of the initial design with black elements indicating material type a and white elements representing material type b.

(b) View for a 3x3 Array of the repeating unit cell.

Figure 3.7: Initial design with two different types of material, denoted as the black and the white elements, distributed over the design space. The unit cell has a base length of 0.02 m. Figures are adopted from Sigmund and Jenson [29]

3.4 Formulation of the Thesis Problem

The problem of interest for this thesis is maximizing the frequency range of a band gap in an infinite periodic sandwich beam near targeted eigenfrequencies to achieve noise filtering. At the same time, the structure must maintain adequate stiffness, and it is preferable to have as low mass as possible. The sandwich beam has two face sheets with predetermined thickness and a core to be designed through density-based topology optimization. Since material for the face sheets is often chosen to be of high stiffness value, the bending stiffness of the sandwich beam is of less concern because the stiff face sheets can sustain the bending. Shear stiffness relies on the geometry of a core made of compliant material, and thus the shear stiffness of the structure must be maintained during the design. The analysis of the sandwich beam can be reduced to the analysis of a unit cell because of the periodicity. The unit cell has the same geometry as the one presented in Figure 3.1. The uniform shear loading acting on the top plate along with the constrained boundary condition imposed on the bottom plate shown in the figure are for calculating the compliance constraint. For the Floquet-Bloch analysis of the unit cell, no external force or constrained boundary condition is imposed, and only the periodic boundary condition is required. A volume constraint is also imposed to restrict the maximum allowable mass to be added to the sandwich structure during the optimization process. The overall optimization problem can be represented as:

$$\text{Problem:} \quad \min_{\mathbf{x}} \quad \frac{1}{\text{Band Gap}} = \frac{\sum_{l=1}^{Q}\sum_{i=b+1}^{J} w_{li}\lambda_i(\mathbf{k}_l) + \sum_{l=1}^{Q}\sum_{i=1}^{b} \hat{w}_{li}\lambda_i(\mathbf{k}_l)}{\sum_{l=1}^{Q}\sum_{i=b+1}^{J} w_{li}\lambda_i(\mathbf{k}_l) - \sum_{l=1}^{Q}\sum_{i=1}^{b} \hat{w}_{li}\lambda_i(\mathbf{k}_l)}$$

$$\begin{aligned}
\text{Subject to :} \quad & c(\mathbf{x}) = \mathbf{U}^T\mathbf{K}\mathbf{U} = \textstyle\sum_{j=1}^{N} x_j^p \mathbf{u}_j^T \mathbf{k}_j \mathbf{u}_j < c_{\max} \\
& \sum_{j=1}^{n} x_j \leq 0.3 \\
& \Phi_i^T \mathbf{T}^H \left(\mathbf{K} - \lambda_i(\mathbf{x})\mathbf{M}\right)\mathbf{T}\Phi_i = \mathbf{0} \quad \text{for} \quad i = 1, ..., J \\
& \Phi_i^T \mathbf{T}^H \mathbf{M}\mathbf{T}\Phi_m = \delta_{im} \quad \text{for} \quad i, m = 1, ..., J \\
& 0.001 \leq x_j \leq 1 \quad \text{for} \quad j = 1, ..., n
\end{aligned} \tag{3.11}$$

where $c_{\max}$ is set as the optimized result obtained from compliance optimization problem, and its corresponding design will be provided as an initial point for the

optimization. Inspired by Kurtze and Watters [20], the top and bottom elements representing the face sheets will use stiff material, and the core will be filled with compliant material. Material properties are given in Table 3.3. To prevent large numbers that cannot be handled properly by MATLAB, the material properties are scaled by a factor of 10^{-11} in the calculation.

Material	E	ρ	ν
Stiff face	70Gpa	3 kg/m^3	0.3
Soft core	10Gpa	1 kg/m^3	0.3

Table 3.3: Material properties for the face sheet and the core.

The main optimization process remains similar to the previous problems with minor changes as given in Figure 3.8. The optimization problem aims to distribute the compliant material with constant mass throughout the core to generate a stiff enough structure with an optimal band gap. In order to prevent intermediate densities, the SIMP method introduced in section 3.2 is used in step 3. In step 4 and 5, the Floquet-Bloch problem and the constraint problem are treated separately since one has Floquet-Bloch boundary conditions and the other has restricted motion at the bottom nodes. Since only a 2-dimensional beam is considered, the periodicity exists along one direction only, and thus the wave vectors are searched from 0 to $i\frac{\pi}{a}$, where a is the distance between neighbouring cells. In step 6, the filtering technique follows Sigmund's mesh independent method [36] introduced in subsubsection 2.7.2.1. Optimization is performed using the same MMA algorithm, and the program exists when design variables $\mathbf{x}$ cease to have changes greater than 0.0005.

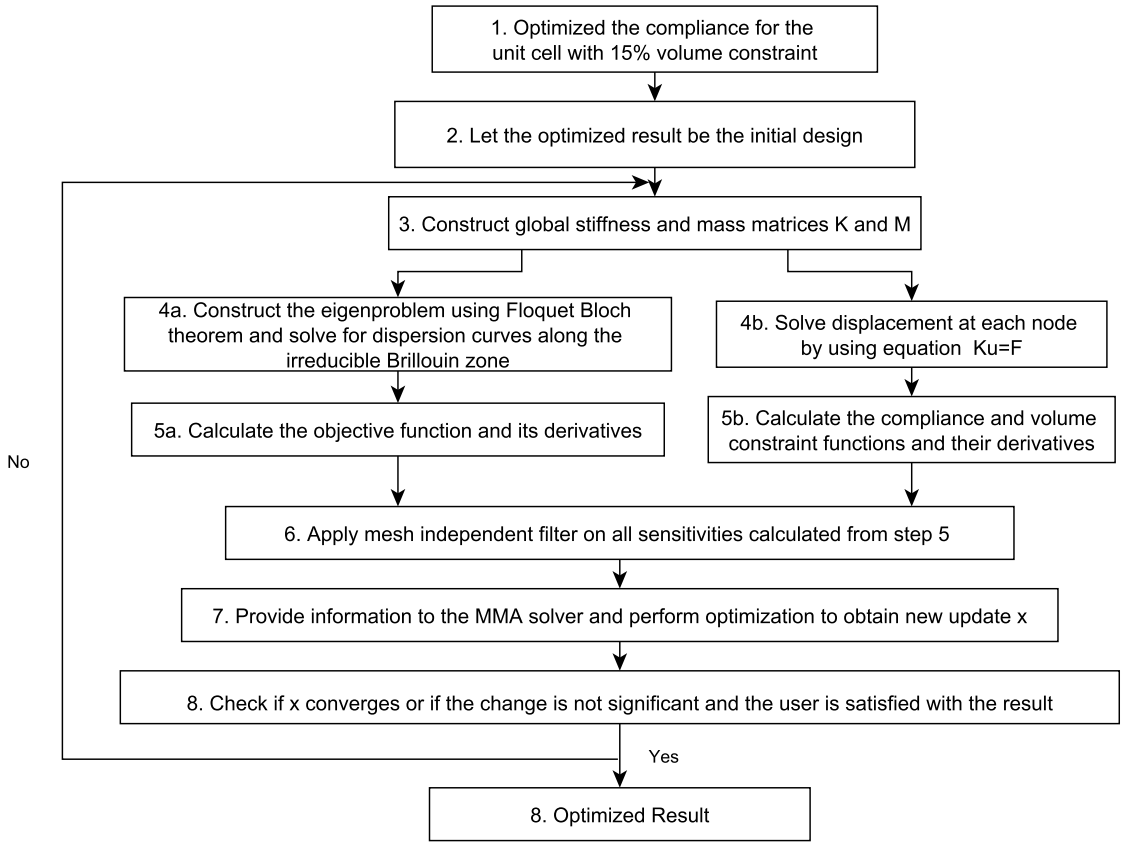

Figure 3.8: Optimization procedure for band gap problem.

Chapter 4

Code Validation Results

4.1 Compliance optimization using both MMA and OC

Compliance optimization is the first problem to be considered for testing the optimization algorithm. Optimized results obtained by using a MMA solver are compared to results obtained by optimality criteria (OC) method in Figure 4.1 to Figure 4.3. The OC method solves the optimality conditions directly when closed-form solutions exist for the problem. Optimality conditions such as Kuhn-Tucker optimality conditions are often used. Because the optimality criteria method is limited to problems that possess a closed-form solution, it is not suitable for the main work of this thesis [21]. The OC algorithm used here is written by Sigmund [35]. From Figure 4.1 to Figure 4.3, it is evident that the topologies obtained using either method have very similar structures and their optimized values agree closely. This indicates that the algorithm written by the author is performing well for this problem. In addition, the resulting truss structure is commonly seen in practice which is another good indication that the algorithm is performing as expected.

MMA relies on asymptotes and move limits to solve the alternative convex subproblem, therefore it is critical to assign the right asymptotes and move limits to the solver each time when running an optimization problem. From observation, it has been noticed that for different problems there are certain combinations of parameters that will result in better performance such as faster convergence. In some cases, if the parameters are not set properly, the problem will either end up searching endlessly in

an infeasible region where the constraints are violated or oscillate without convergence. Thus, for large problems, it appears to be a good idea to run a parameter sweep on a smaller representative problem to get a satisfactory set of parameters to provide fast and reliable convergence.

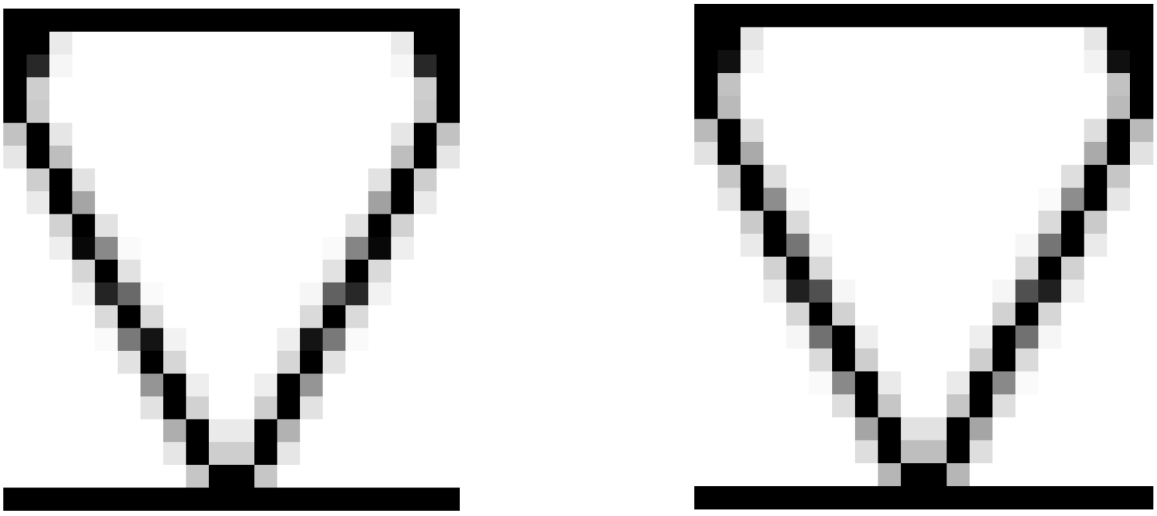

(a) MMA 22x20 Optimized Result: 4.9×10^5

(b) OC 22x20 Optimized Result: 4.6×10^5

Figure 4.1: Optimized compliance results with volume constraint of 15% and with a mesh size of 22x20

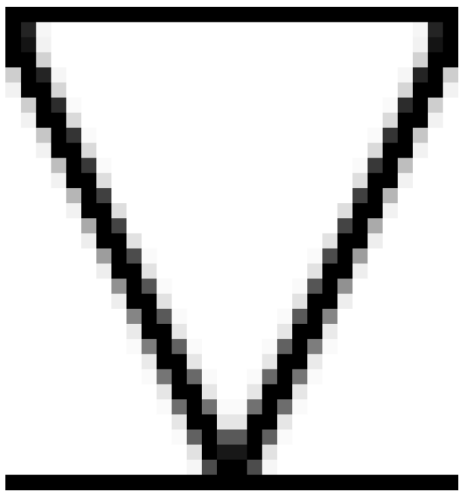

(a) MMA 32x30 Optimized Result: 7.0×10^5

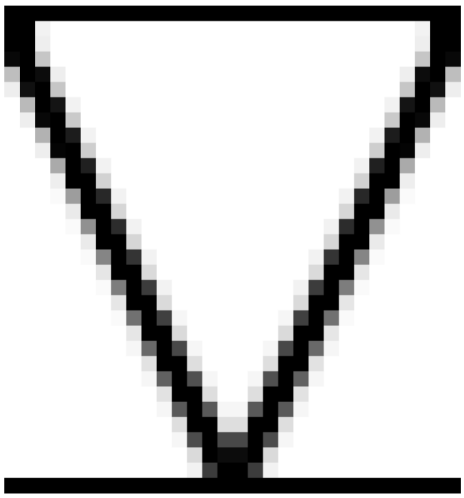

(b) OC 32x30 Optimized Result: 6.8×10^5

Figure 4.2: Optimized compliance results with volume constraint of 15% and with a mesh size of 32x30

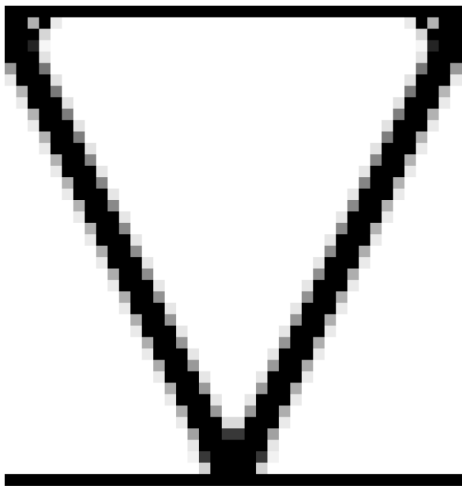

(a) MMA 42x40 Optimized Result: 1.0×10^6

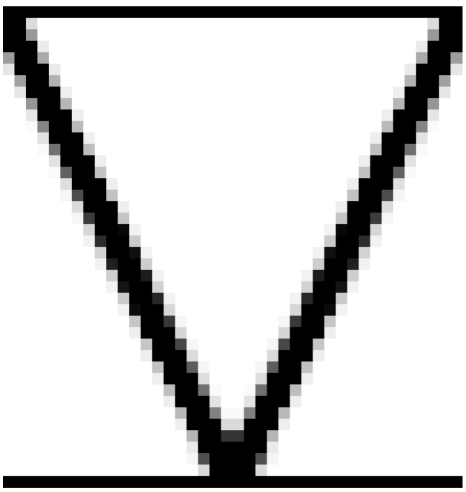

(b) OC 42x40 Optimized Result: 1.0×10^6

Figure 4.3: Optimized compliance results with volume constraint of 15% and with a mesh size of 42x40

4.2 Maximizing the minimum eigenvalue of a 2-dimensional beam

This section presents the result for the minimum eigenvalue maximization problem. The optimal structure obtained by the author is shown in Figure 4.4 with the maximized first eigenfrequency 457.6 rad/s, which is compared to the result obtained by Du and Olhoff [18] with maximized first eigenfrequency 456.4 rad/s. It is noticeable that the two optimized results are not exactly the same. However since Du and Olhoff have not specified the values used for the MMA solver, it is hard for the author to obtain their exact topology. Thus a slightly differing result is expected since the objective function has multi-modality and could have multiple local minima. However, the fact that the optimized eigenvalues agree closely to each other indicates that the optimization algorithm developed by the author is reliable.

Figure 4.4: Optimized structure with the minimum eigenvalue maximized. ω_{1max} = 457.6 rad/s with a 40 x 320 grid size, without post-processing.

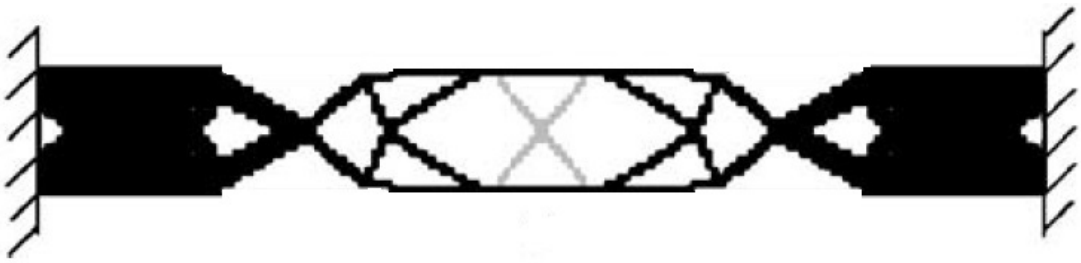

Figure 4.5: Optimized structure with the minimum eigenvalue maximized from literature with ω_{1max} = 456.4 rad/s, and the grid size is not mentioned [18].

4.3 Band Gap Optimization Validation with Sigmund's Work

The results presented in this section are for the same band gap optimization for photonic material considered by Sigmund and Jenson in 2003 [29]. The optimized photonic material obtained by the author is shown in Figure 4.6 and the design obtained by Sigmund and Jenson is shown in Figure 4.7. The difference between the two optimized topologies is a result of the difference in symmetry constraint. While Sigmund and Jenson have imposed square symmetry to the design space, the author has not. The grey elements in the optimal design in Figure 4.6 are caused by applying the SIMP approach, and they can be reduced by turning off the density filter when the design is close to convergence. However, during the iteration, it is hard to determine if a design has entered a shallow region or is close to convergence, and thus the filter has not been adjusted accordingly, causing the final design to have grey elements presented on the corners. The corresponding dispersion curves for both designs are shown in Figure 4.8. The band gap size is calculated as $\frac{\triangle f}{f_0}$, with f_0 being the maximum frequency of the lower band. The band gap size is 0.257 for the optimal design obtained by the author and is 0.21 for the one obtained by Sigmund and Jenson. With larger degrees of freedom as a result of not imposing square symmetry, the maximized band gap size obtained by the author is higher than the one obtained by Sigmund and Jenson, which is expected. Since the computational code is performing the expected band gap maximization, it is believed that the code is performing well, thus no further adjustment is made to arrive at the exact solution.

Lastly, the dispersion curves for the original design shown in 4.9(a) are calculated by the author to compare with the dispersion curves obtained by Sigmund and Jenson in 4.9(b) to confirm that the Floquet-Bloch analysis is accurate.

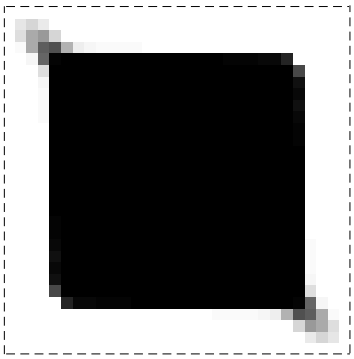

Figure 4.6: Optimized Design by the author without imposing square symmetry has a band gap size of 0.257.

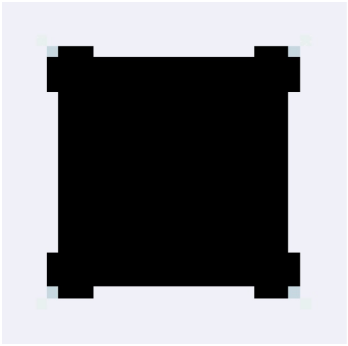

Figure 4.7: Optimized Design by Sigmund and Jenson with imposed square symmetry has a band gap size of 0.21, adopted from [29].

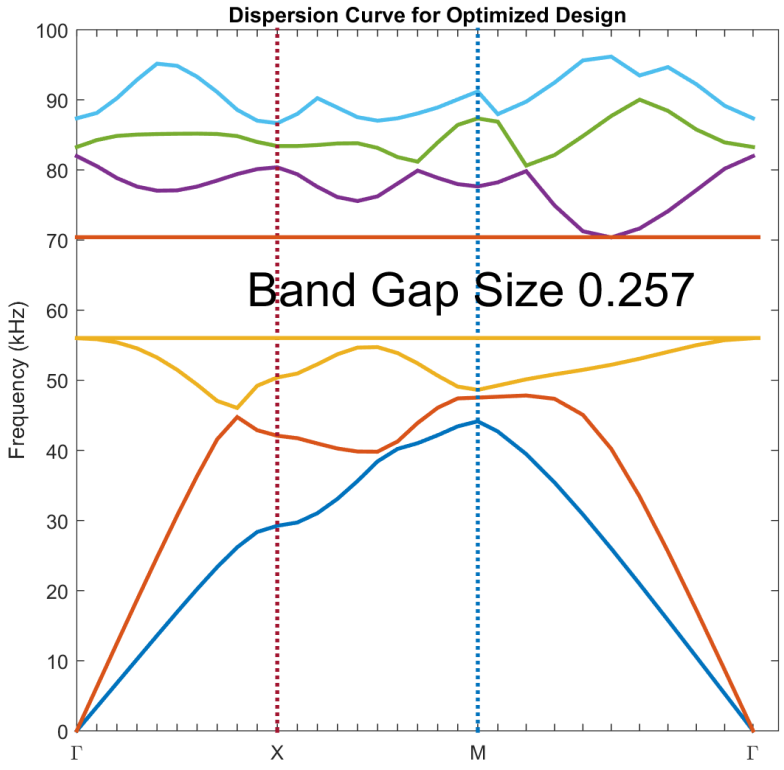

(a) Dispersion curves for the optimized design obtained by the author.

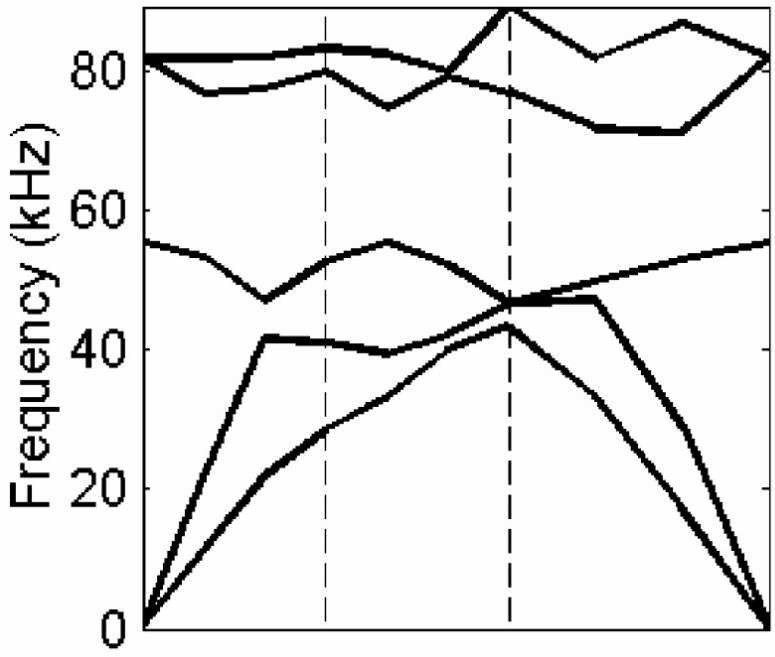

(b) Dispersion curves for the optimal design obtained by Sigmund and Jenson with band gap size = 0.21, adopted from [29].

Figure 4.8: Dispersion curves of the optimized design

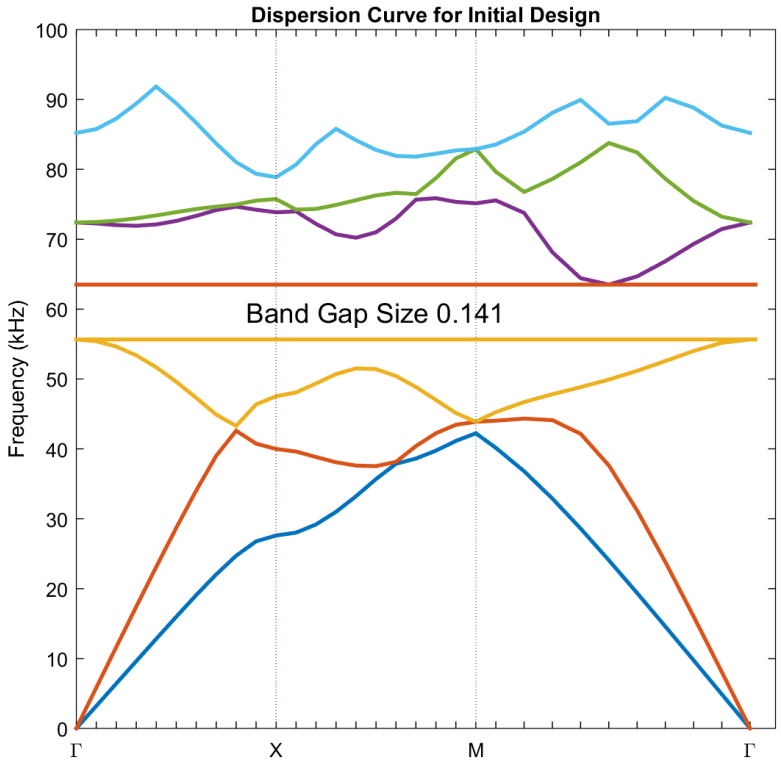

(a) Dispersion curves of the initial design obtained by the author with a band gap size of 0.14.

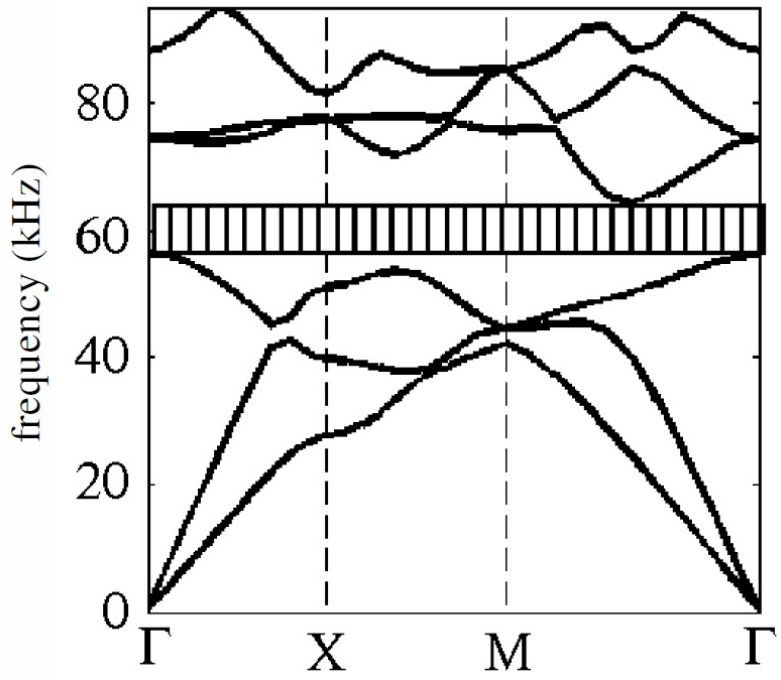

(b) Dispersion curves of the initial design obtained by Sigmund and Jenson with a band gap size of 0.14. Figure is adopted from [29].

Figure 4.9: Dispersion curves for the initial design

Chapter 5

Results and Discussions for Acoustic Sandwich Panels

The main results for a 2-dimensional periodic sandwich beam with a maximized band gap between the third and the fourth band are summarized in this chapter. Two different grid sizes, 22x20 and 32x30, are considered, and their results are presented separately in section 5.1 and section 5.2, respectively. A summary of both results is presented in section 5.3.

5.1 Band Gap Maximization of a Sandwich Beam with 22x20 Grid Size

The initial and optimal designs of a sandwich beam with a grid size of 22x20 are given in Figure 5.1 and 5.2, along with their band structures. The band gap has been maximized from -42.73 Hz to 63.2 Hz, and the structure has undergone dramatic changes to arrive at the optimal design. In order to understand the nature of the optimal design, the mode shapes at the maximum point in the third band (the third mode) and the minimum point in the fourth band (the fourth mode) are shown in Figure 5.3. To maximize the band gap, it is desired to decrease the peak frequency of the third mode and increase the lowest frequency of the fourth mode. Therefore, it is desired to have lower stiffness and higher mass for the moving degrees of freedom in the third mode, and the opposite for the fourth mode. Using this rule-of-thumb, some observations may be made in regard to the design of the optimal structure. This

analysis is not straightforward however an explanation for all the topological features cannot be reasoned entirely from these mode shapes alone, and this is due to the additional constraints placed on the structure as well as the fact that changing the structure changes the dispersion curves such that the modes of interest may vary at the same time. However some notable observations will be made.

First, from the mode-shape plots in Figure 5.3, it can be seen that the third and the fourth modes have similar moving elements circled in red. The moving elements are rotating substantially in the third mode however there is little rotation of these elements in the forth mode, instead it is evident that the elements are under axial tension or compression through their connection to the plate in the forth mode. Evidently these elements are connected to the main structure via a very thin structure effectively acting as a pin connection (connected through a single node) which gives little stiffness to the rotation seen in the third mode while high stiffness to the elongation seen in the forth mode. Additionally it is evident that the elements circled in blue are structural members that are necessary for meeting the compliance constraint.

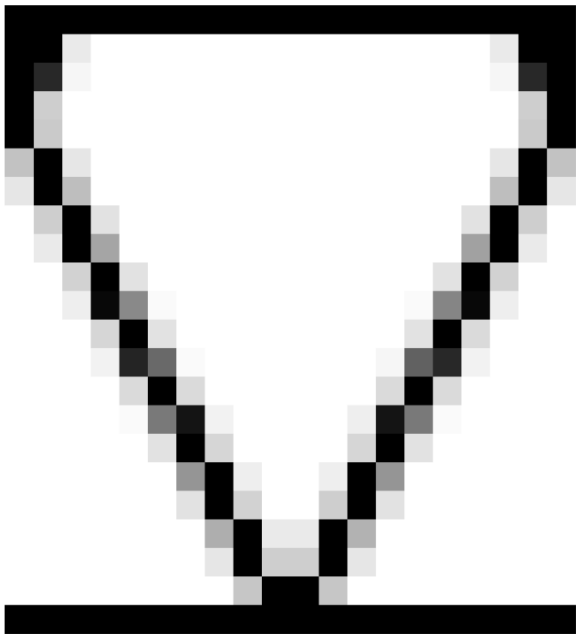

(a) Unit cell of the initial design with a 22x20 grid size.

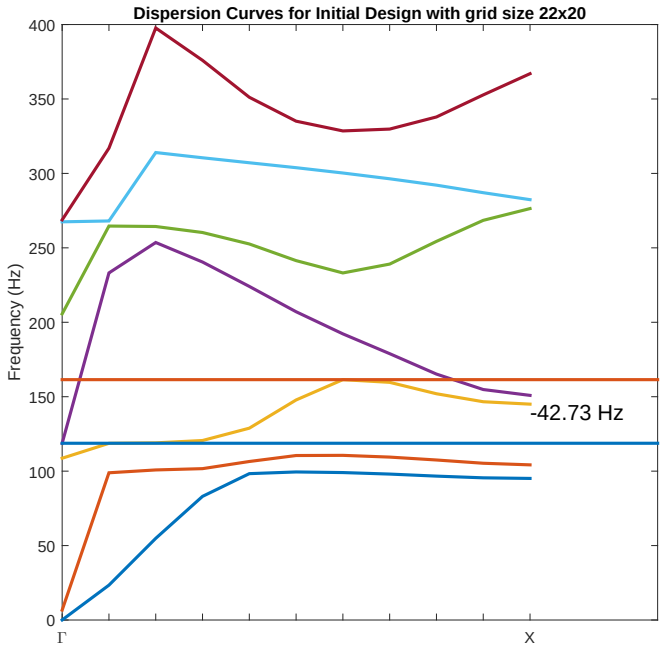

(b) Dispersion Curves for the initial design, showing a negative band gap of -42.73 Hz.

Figure 5.1: Unit cell of the initial design with its dispersion curves shown at the bottom.

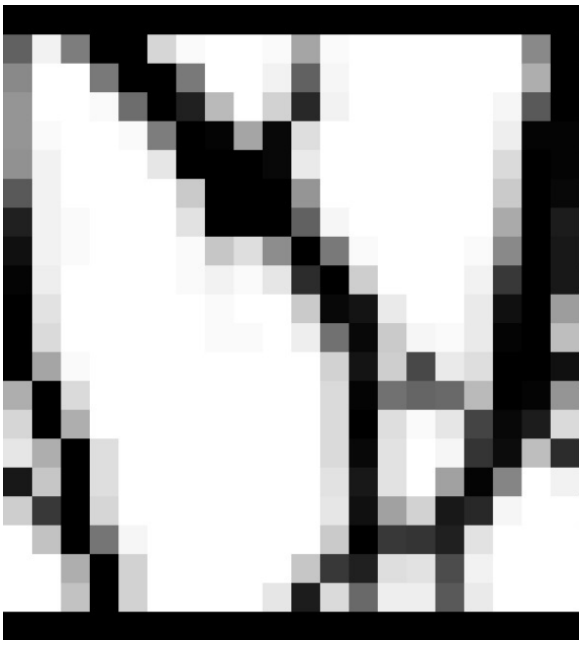

(a) Unit cell of the optimized design with a 22x20 grid size.

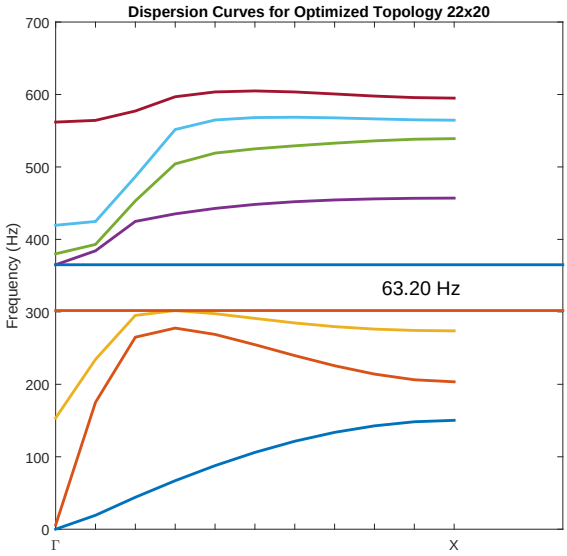

(b) Dispersion Curves for the optimal design, showing a band gap of 63.2 Hz

Figure 5.2: Unit cell of the optimized design with its dispersion curves shown at the bottom.

(a) Patterned structure of the optimal design.

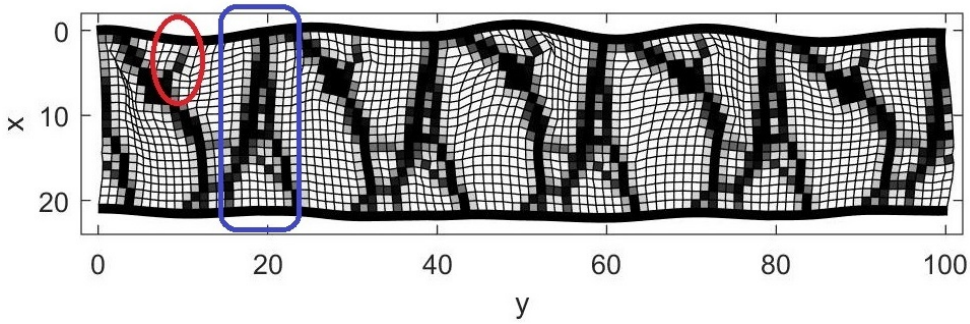

(b) Mode shape corresponding to the peak frequency of the third frequency band.

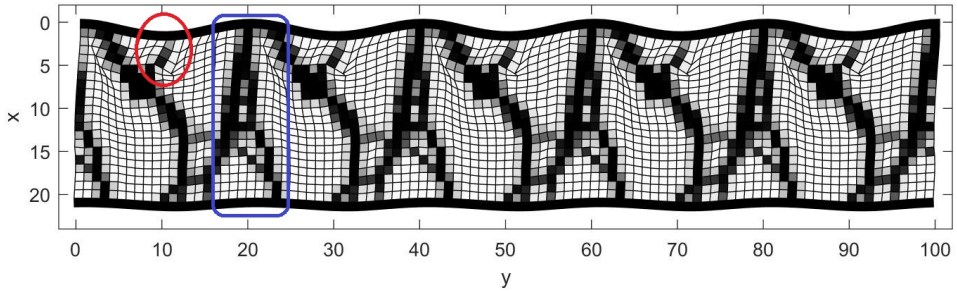

(c) Mode shape corresponding to the lowest frequency of the fourth frequency band.

Figure 5.3: Mode shapes of the structure at the two points that band gap is optimized about. Note that all nodal displacements have been amplified to make the nodal movement visible. Meshes for some elements with low density are highly distorted as a result of the adjustment, no physical overlapping between the nodal points actually occurs.

5.2 Band Gap Optimization of a Sandwich Beam with 32x30 Grid Size

The initial and optimal designs for a 32x30 sandwich beam are presented along with their dispersion curves in Figure 5.4 and 5.5. The band gap has been increased from -13.58 Hz to 59.21 Hz. A periodic patterning and related mode shapes for the sandwich beam are shown in Figure 5.6. Here it is evident that in the third mode, the circled area, which is similar looking to a knee, is made flexible in the middle for the mass on the top to rotate more freely, decreasing the stiffness in the motion of the third mode shape forcing its frequency to decrease. Conversely, the forth mode shape does not incorporate any bending at this position therefore this compliance does not affect the frequency of the forth mode.

Additionally, it may be noted that the movement of the third mode is primarily at the top half of the structure while the motion in the fourth mode is primarily at the bottom half. Observing the structure holistically, the mass of the structure is biased towards the top as seen in 5.6(d) which aligns with the goals of the optimization by adding inertia to the moving degrees of freedom of the third mode while decreasing the inertia of the motion in the fourth mode, thus increasing the band gap.

Lastly, it is evident that the optimized design has similar diagonal members to the original design, which are used to maintain the shear stiffness in order to meet the compliance constraint.

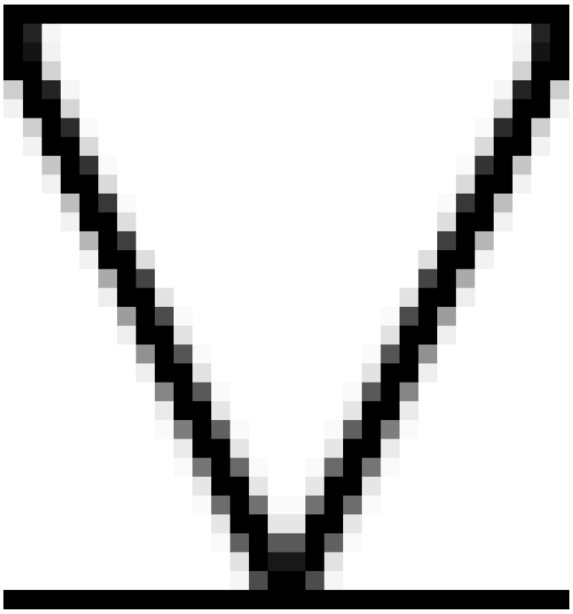

(a) Unit cell of the initial design with a 32x30 grid size.

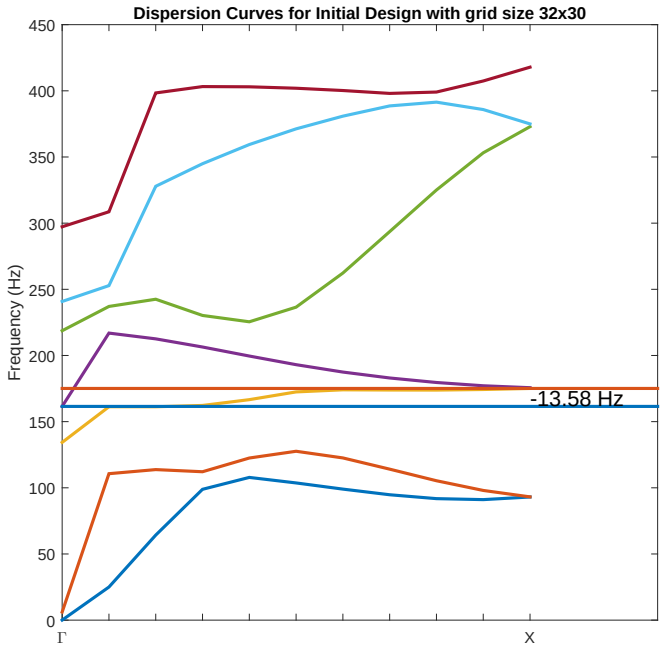

(b) Dispersion Curves for the initial design, showing a negative band gap of -13.58 Hz.

Figure 5.4: Unit cell of the initial design with its dispersion curves shown at the bottom.

(a) Unit cell of the optimized design with a 32x30 grid size.

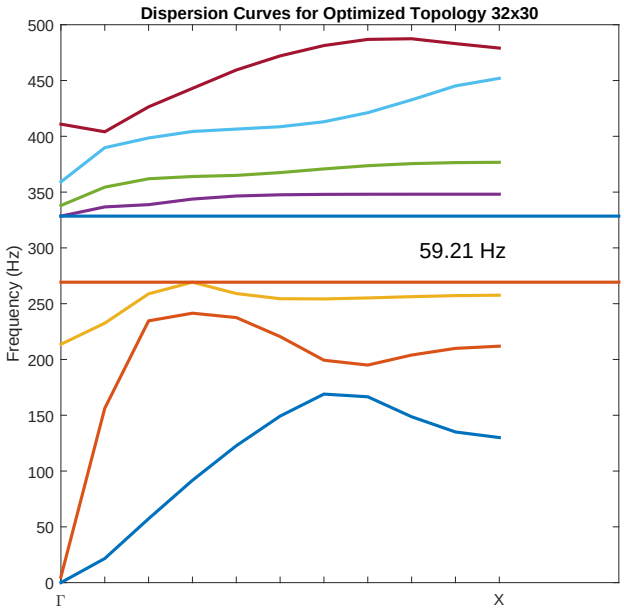

(b) Dispersion Curves for the optimized design, showing a band gap of 59.21 Hz.

Figure 5.5: Unit cell of the optimized design with its dispersion curves shown at the bottom.

(a) Optimal design in repeating pattern.

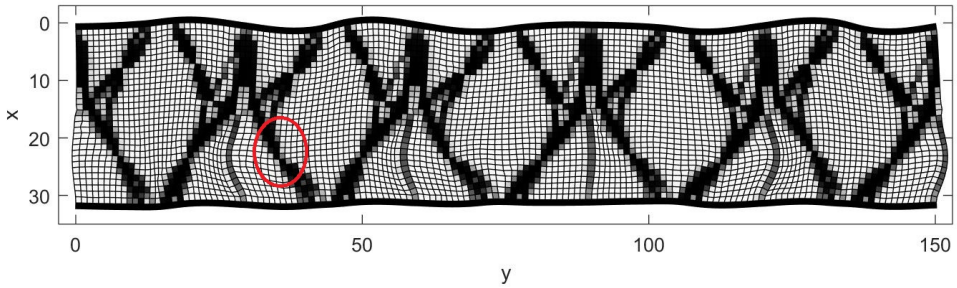

(b) Mode shape corresponding to the maximum point of the third frequency band.

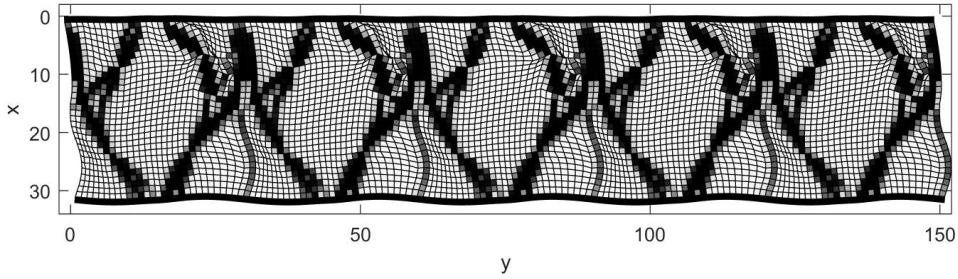

(c) Mode shape corresponding to the minimum point of the fourth frequency band. Note that all nodal displacements have been adjusted by a factor to make the nodal movement noticeable. Meshes for some elements with low density are highly distorted as a result of the adjustment, no physical overlapping between the nodal point actually occurs.

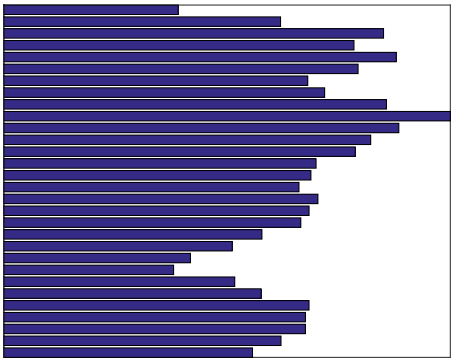

(d) Row-wise mass distribution of the core.

Figure 5.6: Mode shapes of the structure at the two points that band gap is calculated at.

5.3 Summary

The natures of the optimized designs are not intuitive. With the mode shapes plotted for the related modes, one can see how elements behave in each mode. Making use of the fact that the optimizer will aim to maximize the minimum frequency of the fourth band and minimize the maximum frequency of the third band, structures in the major moving parts in each mode can be explained. Moreover, it is noticed that lumped masses appear in both optimal structures and resemble resonators. Resonant elements are often placed inside panels to increase sound transmission loss over a narrow frequency range [9]. An example for this type of structure is shown in Figure 5.7. In the figure, the resonating structures composed of lump masses connected with pins are very similar to the optimal designs, especially to the one with a mesh size of 32x30. This is an important finding for demonstrating that the optimal topologies generated have physical meaning. Furthermore, optimizing the structure's band gap around a frequency range is believed to be equivalent to improving the STL over that frequency range, and the same purpose can be achieved by placing resonant elements inside the structure. This resemblance to existing lumped-mass resonator designs strongly suggests that the topology optimization is performing as expected.

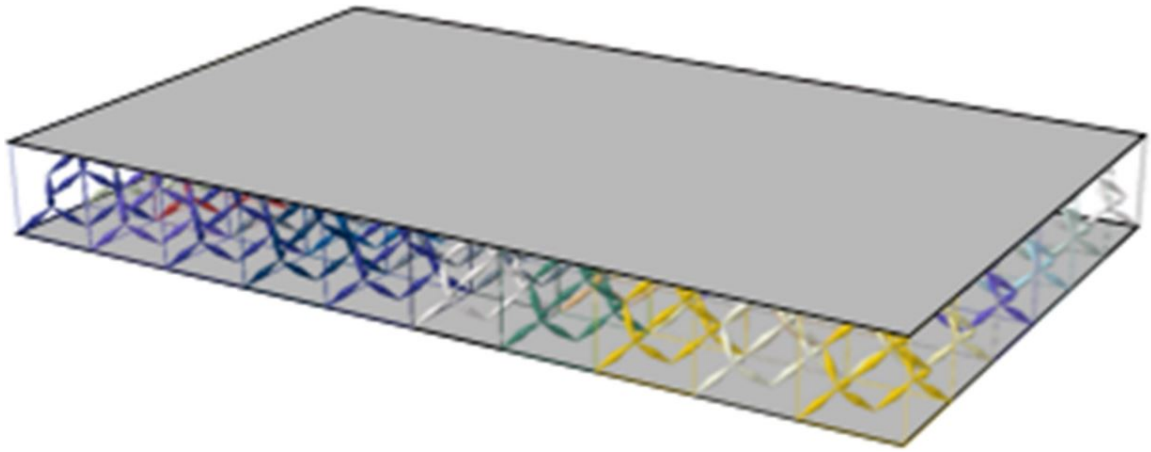

Figure 5.7: Sandwich panel with internal resonating structures which can improve damping performance with minimum weight penalties. (Figure is obtained from the website of the Integrated Multi-field Metamaterial Damping research group in the department of Mechanical and Process Engineering group from Swiss Federal Institute of Technology in Zurich.)

Finally, the optimized topologies with different mesh size are quite distinct. This

can be caused by the following reasons:

1. The optimizer aims to maximize the band gap between the third and the fourth band without a reference point. This can lead to shifting of the whole band structure, meaning that the optimized designs generated from different mesh sizes have band gaps around different frequencies. From the dispersion curves of the two optimal designs shown in Figure 5.2 and Figure 5.5, it can be seen that the first design has a band gap between 300 Hz and 363 Hz and the second design has a band gap between 270 Hz and 330 Hz.

2. The initial design is very different between a 22x20 grid size and a 32x30 grid size. As one can see from Figure 5.1 and Figure 5.4 that the dispersion curves for the two initial designs are rather different even though the major structures are similar.

3. The multi-modality of the problem can trap the optimizer within a local minimum solution. It is believed that the obtained optimum is either a local minimum or a local shallow point. The global optimum is difficult to achieve with the current optimization technique. This is also a reason why different initial conditions can lead to different solutions [29].

To summarize, the results obtained by this thesis have shown interesting topologies with resemblance to resonators, while having a local optimal band gap between the third and the fourth bands and meeting mass and shear stiffness constraints.

Chapter 6

Conclusion

The need for decreasing green house gas emissions in aviation has motivated the search for advanced material for aircraft applications. Light weight acoustic panels for noise attenuation are desirable structural elements. This thesis pursues methods for optimizing a structure for minimal acoustic transmission while remaining light and stiff.

A phenomenon, referred to as a band gap, where no elastic waves can propagate through the structure, has been introduced and studied. By maximizing the band gap around an undesired frequency, sound attenuation can be improved [2, 27]. The author has made use of the band gap analysis in conjunction with topology optimization to improve the acoustic performance of a 2-dimensional sandwich panel within a certain frequency regime. This is a novel contribution. Interesting sandwich structures have been obtained with a band gap maximized between the third and the fourth bands. However, the study is restricted to a 2-dimensional sandwich beam with the optimal band gap located between two predetermined frequency bands. Additionally, multi-modality of the problem is not addressed in this thesis, and there is no guarantee that a global optimum has been found as opposed to a local extremum. Moving this work forward, the study can be brought to a 3-dimensional case with the stop band centered around unwanted frequencies, such as coincidence frequencies, for more practical acoustic applications. In conclusion, the objectives of the thesis has been fulfilled, and there are several suggestions for future work which will be documented below.

6.1 Future Work

1. It is highly recommended to extend the study to a 3-dimensional one in order to construct the sandwich panel and test the sound transmission loss through the panel in laboratory to validate the result.

2. There are many improved versions of MMA that will speed up the convergence [24, 25]. It will be more efficient to implement those versions once the design space has been increased to a 3-dimensional one.

3. Gradient-based search methods usually encounter local optimality, especially with multi-modal problems, and that has eliminated the possibility of exploring the global optimum. Multi-Start strategies are proposed to prevent the solution to be trapped in a local region [26]. It is highly recommended to implement the strategy to overcome the local optimality situation.

Appendices

A Finite Element Approach

To transform the governing equations into the analytical form in Equation 2.15, one has to obtain the weak form from the strong form by the following strategy. Take Equation 2.11 for example, by only considering wave propagation in the x-y plane and assuming any material properties only vary along the x-y plane, i.e $\rho = \rho(x, y)$, $\lambda = \lambda(x, y)$, and $\mu = \mu(x, y)$, the form in Equation 2.11 can be reduced to:

$$\text{Strong Form}: \quad \rho\frac{\partial^2 u}{\partial t^2} = \frac{\partial}{\partial x}\left((2\mu+\lambda)\frac{\partial u}{\partial x} + \lambda\frac{\partial v}{\partial y}\right) + \frac{\partial}{\partial y}\left(\mu\left(\frac{\partial u}{\partial y} + \frac{\partial v}{\partial x}\right)\right) \quad (1)$$

A test function ν of the following properties will be added to both side of the equation.

$$\nu(0) = 0 \quad (2)$$

Assuming no external force acting on the system, the following boundary conditions can be obtained.

$$\left.\frac{\partial u}{\partial x}\right|_{\partial\Omega} = 0, \qquad \left.\frac{\partial v}{\partial y}\right|_{\partial\Omega} = 0 \quad (3)$$

The weak form is constructed by integrating Equation 1 with the test function multiplied on both sides.

$$\oint \nu\rho\frac{\partial^2 u}{\partial t^2}d\Omega = \oint \nu\frac{\partial}{\partial x}\left((2\mu+\lambda)\frac{\partial u}{\partial x} + \lambda\frac{\partial v}{\partial y}\right)d\Omega + \oint \nu\frac{\partial}{\partial y}\left(\mu\left(\frac{\partial u}{\partial y} + \frac{\partial v}{\partial x}\right)\right)d\Omega \quad (4)$$

Equation 4 can be further reduced by applying integration by parts on the right hand size. In the end, the following weak form is obtained:

$$\oint \nu\rho\frac{\partial^2 u}{\partial t^2} = -\oint \frac{\partial\nu}{\partial x}\left((2\mu+\lambda)\frac{\partial u}{\partial x} + \lambda\frac{\partial v}{\partial y}\right) - \oint \frac{\partial\nu}{\partial y}\left(\mu\left(\frac{\partial u}{\partial y} + \frac{\partial v}{\partial x}\right)\right) \quad (5)$$

Apply similar approach for the governing equation along the y direction and get

$$\oint \nu\rho\frac{\partial^2 v}{\partial t^2} = -\oint \frac{\partial\nu}{\partial x}\left(\mu\left(\frac{\partial v}{\partial x} + \frac{\partial u}{\partial y}\right)\right) - \oint \frac{\partial\nu}{\partial y}\left((2\mu+\lambda)\frac{\partial v}{\partial y} + \lambda\frac{\partial u}{\partial x}\right) \quad (6)$$

Assume the solution and test function are of the following form

$$u = \sum_{i=1}^{m} a_i N_i e^{iwt} \quad v = \sum_{i=1}^{m} a_i N_i e^{iwt} \quad \text{and} \quad \nu = \sum_{i=1}^{m} a_i N_i \quad (7)$$

where a_i are undetermined coefficients and N_i are the shape functions. For plate elements, the following Isoparametric Quadrilateral Shape functions are being used.

$$\begin{aligned} N_1(\zeta,\eta) &= 0.25(1-\zeta)(1-\eta) \\ N_2(\zeta,\eta) &= 0.25(1+\zeta)(1-\eta) \\ N_3(\zeta,\eta) &= 0.25(1+\zeta)(1+\eta) \\ N_4(\zeta,\eta) &= 0.25(1-\zeta)(1+\eta) \end{aligned} \tag{8}$$

The shape function transforms the values from physical coordinate (x, y) into an Isoparametric coordinate (ζ, η), i.e

$$x(\zeta,\eta) = \mathbf{Nx} \quad = \quad y(\zeta,\eta) = \mathbf{Ny} \tag{9}$$

The derivative of $\mathbf{N}$ with respect to the physical coordinate (x, y) has the following form:

$$\begin{bmatrix} \dfrac{\partial N_i}{\partial x} \\ \\ \dfrac{\partial N_i}{\partial y} \end{bmatrix} = \mathbf{J}^{-1} \begin{bmatrix} \dfrac{\partial N_i}{\partial \zeta} \\ \\ \dfrac{\partial N_i}{\partial \eta} \end{bmatrix} \tag{10}$$

with the Jacobian matrix being:

$$\mathbf{J} = \begin{bmatrix} \dfrac{\partial x}{\partial \zeta} & \dfrac{\partial y}{\partial \zeta} \\ \\ \dfrac{\partial x}{\partial \eta} & \dfrac{\partial y}{\partial \eta} \end{bmatrix} \tag{11}$$

A complete matrix for derivative of $\mathbf{N}$ in the physical coordinate (x, y) is denoted

as $\mathbf{H}$

$$\mathbf{H} = \begin{bmatrix} \frac{\partial N_1}{\partial x} & 0 & \frac{\partial N_2}{\partial x} & 0 & \frac{\partial N_3}{\partial x} & 0 & \frac{\partial N_4}{\partial x} & 0 \\ 0 & \frac{\partial N_1}{\partial y} & 0 & \frac{\partial N_2}{\partial y} & 0 & \frac{\partial N_3}{\partial y} & 0 & \frac{\partial N_4}{\partial y} \\ \frac{\partial N_1}{\partial y} & \frac{\partial N_1}{\partial x} & \frac{\partial N_2}{\partial y} & \frac{\partial N_2}{\partial x} & \frac{\partial N_3}{\partial y} & \frac{\partial N_3}{\partial x} & \frac{\partial N_4}{\partial y} & \frac{\partial N_4}{\partial x} \end{bmatrix} \tag{12}$$

With the shape function and its derivative being constructed, the weak forms in Equation 5 and Equation 6 can be assembled into a system of coupled equations:

$$\left(\mathbf{K} - w^2\mathbf{M}\right)\mathbf{a} = 0 \tag{13}$$

where $\mathbf{K}$ and $\mathbf{M}$ are globally assembled matrices from the element matrix being calculated as:

$$\mathbf{K}_e = \oint \mathbf{H}^T\mathbf{D}\mathbf{H}d\Omega \tag{14}$$

$$\mathbf{M}_e = \oint \rho\mathbf{N}^T\mathbf{N}d\Omega \tag{15}$$

with the flexural rigidity matrix $\mathbf{D}$ being

$$\mathbf{D} = \begin{bmatrix} 2\mu + \lambda & \lambda & 0 \\ \lambda & 2\mu + \lambda & 0 \\ 0 & 0 & \mu \end{bmatrix} \tag{16}$$

Additionally, because of the conversion from physical to isoparametric coordinates, the stiffness matrix $\mathbf{K}_e$ and the mass matrix $\mathbf{M}_e$ can be solved using Gauss Quadrature method. The Gauss Quadrature method is shown as

$$\mathbf{K}_e = \sum_{j=1}^{n_{gp}}\sum_{i=1}^{n_{gp}} W_j W_i J\left(\zeta_i, \eta_j\right)\mathbf{H}\left(\zeta_i, \eta_j\right)^T\mathbf{D}\mathbf{H}\left(\zeta_i, \eta_j\right) \tag{17}$$

$$\mathbf{M}_e = \sum_{j=1}^{n_{gp}}\sum_{i=1}^{n_{gp}} \rho W_j W_i J\left(\zeta_i, \eta_j\right)\mathbf{N}\left(\zeta_i, \eta_j\right)^T\mathbf{N}\left(\zeta_i, \eta_j\right) \tag{18}$$

where W_i and W_j are the weights for the gauss points ζ_i and η_j.

In summary, this section has introduced a finite element formulation of the dynamic system of wave propagation in a 2-dimensional plane. By applying the Floquet-Bloch theorem to the dynamic system as introduced in the previous subsection 2.4.1 and solving for the dispersion curves along Brillouin zone, the partial or complete band gap for the periodic structure can be obtained.

References

[1] D. Tidman A. Olason. Methodology for topology and shape optimization in the design process. Master's thesis, CHALMERS UNIVERSITY OF TECHNOLOGY, 2010.

[2] J. Woodhouse A. Srikantha Phani and N. A. Fleck. Wave propagation in two-dimensional periodic lattices. *Acoustical Society of America*, 2006.

[3] J.F Allard. Propagation of sound in porous media - modelling sound absorbing materials. *New York, Elsevier Applied Science*, 1993.

[4] E. Lund A.P. Seyraniant and N. Olhoff. Multiple eigenvalues in structural optimization problems. *Structural Optimization*, 8, 207-227 1994.

[5] C. K. Barton and J. S Mixson. Noise transmission and control for light twin-engine aircraft. *J. Aircr.,*, 18(7), 570-575.

[6] H. Baumgartl. Lightweight, versatile all-rounder. *Kunststoffe international*, 4 (2006) 74-78.

[7] W. V Bhat. Flight test measurement of measurement of exterior turbulent boundary layer pressure fluctuations on boeing model 737 airplane. *Journal of Sound and Vibration*, 1971.

[8] Ulla Biernat. Basf foam in the interior insulation of new boeing aircraft. *Aircraft Engineering and Aerospace Technology*, 80 (2008) ss:1.

[9] L.A. Lazarev B.M. Efimtsov. Sound transmission loss of panels with resonant elements. *Acoustical Physics*, Vol. 47, No. 3, 2001, pp. 291-296.

[10] P. Allinger C.B.W. Pedersen. Industrial implementation and applications of topology optimization and future needs. *IUTAM Symposium on Topological Design Optimization of Structures, Machines and Materials: Status and Perspectives*, 2006, p 229-238.

[11] B.H Jia F. Menga, X.D Huang. Bi-directional evolutionary optimization for photonic band gap structures. *Journal of Computational Physics*, 302(2015)393-404.

[12] K. A. Finnegan. Carbon fiber composite pyramidal lattice structures. Master's thesis, University of Virginia, 2007.

[13] Cunefare K.A Franco F., Ruzzene M. Structural-acoustic optimization of sandwich panels. *Journal of Vibration and Acoustic*, (2007) 129, 330-340.

[14] F. W. Grosveld and J. S Mixson. Noise transmission through an acoustically treated and honeycomb-stiffened aircraft sidewall. *J. Aircr.,*, 22(5), 434-440.

[15] IATA. Annual review 2013. technical report. *International Air Transportation Association*, 2013.

[16] Pennig S. Quehl J. and Rolny V. Effects of aircraft cabin noise on passenger comfort. *Ergonomics*, 2012 55(10) 1252-1265.

[17] H.S Jr J.C. Molina, J.Fiorelli. Analysis of the stresses in corrugated sheets under bending. *Materials Research*, 2014; 17(2): 338-345.

[18] Niels Olhoff Jianbin Du. Topological design of freely vibrating continuum structures for maximum values of simple and multiple eigenfrequencies and frequency gaps. *Struct Multidisc Optim*, (2007) 34:91-110.

[19] C. Kittel. *Elementary Solid State Physics: A Short Course, 1st ed.* Wiley, New York, 1962.

[20] G. Kurtze and B. G Watters. New wall design for high transmission loss or high damping. *Journal of the acoustical society of America*, (1959) 31(6), 739-748.

[21] W. Yang LZ. Yin. Optimality criteria method for topology optimization under multiple constraints. *Computers and Structures*, (2001) 1839-1850.

[22] Ruzzene M. Vibration and sound radiation of sandwich beams with honeycomb truss core. *Journal of sound and vibration*, (2004) 277, 741-763.

[23] Ruzzene. M. Structural and acoustic behaviour of chiral truss-core beams. *Journal of sound and vibration*, (2006) 128, 616-626.

[24] S. A. Santos M. A. Gomes-Ruggiero, M. Sachine. Globally convergent modifications to the method of moving asymptotes and the solution of the subproblems using trust regions: theoretical and numerical results. Revised Version December 3, 2010.

[25] A. Guessab M. Bachar, T. Estebenet. A moving asymptotes algorithm using new local convex approximation methods with explicit solutions. *Electronic Transactions on Numerical Analysis*, Volume 43, pp. 21-44, 2014.

[26] R. Mart. Multi-start methods. University of Valencia. Spain.

[27] E. Moosavimehr. Sound transmission loss characteristics of sandwich panels with a truss lattice core. Master's thesis, The University Of British Columbia, 2015.

[28] Bendsoe MP. Optimal shape design as a material distribution problem. *Struct Optim*, 1989.

[29] J.S Jensen O. Sigmund. Systematic design of phononic band-gap materials and structures by topology optimization. *Phil. Trans. R. Soc. Lond*, A (2003) 361, 1001-1019.

[30] K. Maute O. Sigmund. Toplogy optimiaztion approaches. *Struct*, 2013.

[31] N.L. Pedersen and A.K. Nielsen. Optimization of practical trusses with constraints on eigenfrequencies, displacements, stresses, and buckling. *Struct Multidisc Optim*, 25, 436-445 (2003).

[32] Chen Yuan Huang Qibai and Hanmin Shi. An investigation on the physiological and psychological effects of infrasound on persons. *Journal of low frequency noise vibration and active control 23*, (2004) 71-76.

[33] H.J. Rice and R Wilson. Radiation damping in plates, induced by porous media. *Journal of sound and vibration*, (1999) 221(1), 143-167.

[34] M Ruzzene. Vibration and sound radiation of sandwich beams with honeycomb truss core. *Journal of sound and vibration*, (2004) 277, 741-763.

[35] O. Sigmund. A 99 line topology optimization code written in matlab. *Struct Multidisc Optim*, 21, (2001) 120-127.

[36] O. Sigmund. On the design of compliant mechanisms using topology optimization. *MECH. STRUCT. AND MACH*, 25(4), 493-524 (1997).

[37] K. Svanberg. Mma and gcmma, versions september 2007. This note describes the algorithms used in the author's latest implementations of MMA and GCMMA.

[38] K. Svanberg. A globally convergent version of mma without linesearch,. In *the First World Congress of Structural and Multidisciplinary Optimization*, 1995, pp. 916.

[39] K. Svanberg. A class of globally convergent optimization methods based on conservative convex separable approximations. *SIAM J. OPTIM.*, Vol. 12, No. 2, pp. 555-573.

[40] K. Svanberg. The method of moving asymptotes - a new method for structural optimization. *International Journal for Numerical Methods in Engineering*, Vol.24 359-373 (1987).

[41] S Tewes. Active trim panel attachments for control of sound transmission through aircraft structures. *Ph.d thesis, Technischen University Munchen*, 2006.

[42] P. Thamburaj and Q Sun. Optimization of anisotropic sandwich beams for higher sound transmission loss. *J. Sound Vib.,*, 254(1), 23-36.